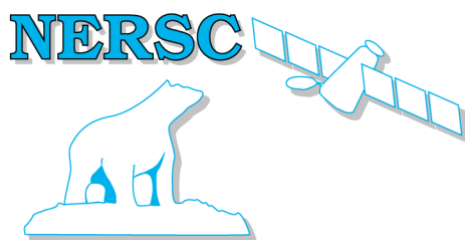


A non-profit  
Research institute affiliated  
With the University of Bergen



Jahnebakken 3  
N-5007 Bergen,  
Norway  
<http://www.nersc.no>

## NERSC Technical report no. 423

# UAK 2021: Cruise and data report



In support to

*UAK project*

Funded by Research Council of Norway

*DAS project*

Funded by Research Council of Norway

*INTAROS project*

Funded by EC H2020



Version 3.0

Date: 19 October 2022

UAK Research school report 2021

<b>TITLE:</b> UAK 2021: Scientific Cruise plan	<b>REPORT IDENTIFICATION</b> NERSC Technical report no. 423
<b>CLIENT</b> Research Council of Norway US Office of naval Research - Global Research and Innovation Action under EC Horizon2020	<b>CONTRACT</b> Project number: 274891, 309708 Grant Agreement no. 727890
<b>CLIENT REFERENCE</b>	<b>AVAILABILITY</b> Open
<b>INVESTIGATORS.</b> <b>Editors: Stein Sandven, Hanne Sagen</b> Contributors: Instructors and young scientists and participating in the UAK 2021 research school.	<b>Approval:</b> 19 October 2022 

### Instructors

Institution and nation.	Name	Expertise	Education/Position
NERSC, Norway	Hanne Sagen (Cruise leader)	Polar research, acoustics, moorings	Dr. Scient/research leader
NERSC, Norway	Stein Sandven (Project leader)	Polar research, sea ice in situ & remote sensing	Professor/Senior Scientist
NERSC, Norway	Espen Storheim	Polar research, acoustics, instrumentation	PhD/Scientist
NERSC, Norway	Torill Hamre	Data management	Dr. Scient/research leader
NERSC, Norway	Frode Monsen	Data management	Programmer
Metno, Norway	Alistair Everett	Glaciology, sea ice forecasting	PhD/Scientist
NORCE, Norway	Tom Rune Lauknes	Sea ice remote sensing and drone technology	PhD/Scientist
IOPAS, Poland	Agnieszka Beszczynska-Möller	Polar research, Oceanography, moorings	Research leader/PhD
ONR – Global, UK	Elena McCarthy	Ocean Acoustics, research programs.	Program officer

### Young Scientists participating in the cruise

Institution and nation.	Name	Scientific discipline	Student
Nansen Center, Norway	Astrid Stallemo	Physical Oceanography	Master S.
University of Bergen, Norway	Anna Mathea Skaar	Ocean technology	Bachelor
University of Bergen, Norway	Mads Skjerven Moldrheim	Ocean technology	Bachelor
University of Bergen, Norway	Guney Dincturk	Marine seismics	Master S.
University of Bergen, Norway	Elinor Tessin	Marine optics	PhD
University of Tromsø, CIRFA, Norway	Anna Telegina	Sea ice	PhD
University of Tromsø, CIRFA, Norway	Laust Færch	Sea ice	PhD
University of Tromsø, CIRFA and Met.no	Jozef Rusin	Sea ice	PhD
Scripps Institution of Oceanography, USA	William Jenkins	Underwater Acoustics	PhD
Scripps Institution of Oceanography, USA	Hayden Allen Johnson	Underwater Acoustics	PhD
University of Colorado Boulder, USA	Meghan Helmberger,	Ocean Climate	PhD
University of Colorado Boulder, USA	Sofia Vakhutinsky	Ocean Climate	Bachelor

## Contents

<b>INTRODUCTION.....</b>	<b>3</b>
WHAT WAS THE AIM OF THE RESEARCH SCHOOL? .....	3
PROJECTS AND PARTIES THAT MADE THE RESEARCH SCHOOL ONBOARD KV SVALBARD POSSIBLE .....	3
<b>1. IN SITU SNOW AND ICE MEASUREMENTS.....</b>	<b>4</b>
1.1. RESEARCH AREA .....	5
1.2. METHODS .....	5
1.2.1. <i>Snow pits</i> .....	5
1.2.2. <i>Thickness drillings</i> .....	5
1.2.3. <i>Ice coring</i> .....	5
1.3. RESULTS.....	5
1.3.1. <i>Snow pits</i> .....	5
1.3.2. <i>Thickness drillings</i> .....	6
1.3.3. <i>Ice cores</i> .....	6
<b>2. ROV WORK UNDER THE ICE.....</b>	<b>8</b>
2.1. FIFISH 6V ROV.....	8
2.2. ROV OPERATION .....	9
2.3. RESULTS.....	10
2.4. ISSUES.....	12
2.4.1. DIFFICULT CONTROL .....	12
2.4.2. APP INTERFACE UNITS .....	12
2.4.3. DATES AND TIMESTAMPS .....	13
2.4.4. BEEPING SOUNDS .....	13
2.4.5. DATA EXPORT .....	13
2.4.6. CLIPPING OF VIDEOS .....	13
2.4.7. CAPTURING PHOTOS.....	13
2.5. FINAL REMARKS.....	13
<b>3. SEA ICE REMOTE SENSING AND IN SITU VALIDATION DATA.....</b>	<b>14</b>
3.1. INTRODUCTION.....	15
3.2 METHODS.....	17
3.2.1 <i>Sea ice classification based on SAR imagery</i> .....	17
3.2.2 <i>Field Data</i> .....	17
3.2.3 <i>Ice coring</i> .....	18
3.2.4 <i>Snow</i> .....	18
3.3 RESULTS.....	18
3.3.1 <i>Snow Height and Temperature</i> .....	20
3.3.2 <i>Salinity</i> .....	21
3.3.3 <i>Ice Temperature</i> .....	21
3.3.4 <i>Classification</i> .....	22
3.4 DISCUSSION .....	26
3.5 REFERENCES .....	27
<b>4. OCEAN OBSERVATIONS .....</b>	<b>28</b>
4.1 CTD DATA .....	28
4.2 INSTRUMENTS, PROCEDURE AND DATA PROCESSING .....	30
4.3 BUOY, INSTRUMENTS, DEPLOYMENT AND RECOVERY.....	30
4.3.1 <i>SBE37 MicroCAT</i> .....	30
4.3.2 <i>Kilo Iridium Beacon</i> .....	32

4.3.4 MTE $\mu$ AURAL.....	33
4.3.5 XMB-11K Radio Beacon.....	33
4.3.6 XMF-11k LED Flasher.....	33
4.3.7 Buoy Deployment.....	34
4.3.8 Buoy Recovery.....	34
4.4 DRIFTERS.....	34
<b>5. ACOUSTIC MEASUREMENTS .....</b>	<b>36</b>
5.1 INTRODUCTION.....	36
5.2 DRIFTER BUOY .....	36
5.2.1 Equipment, Deployment, and Recovery.....	36
5.2.2 Data Analysis.....	37
5.2.3 Drifter Buoy: Highlights.....	39
5.3 ACOUSTIC LOCALIZATION.....	45
5.3.1 Purpose.....	45
5.3.2 Methodology.....	45
5.3.3 Calculations.....	46
5.3.4 Results.....	47
5.4 ICE STATIONS.....	48
5.4.1 Taking a Sounding with Explosives.....	48
5.5 PROPAGATION MODELING .....	49
REFERENCES.....	50
<b>APPENDIX 1: AVAILABLE SATELLITE IMAGES .....</b>	<b>51</b>
1. ICE STATION 1.....	51
2. ICE STATION 2.....	52
<b>APPENDIX 2: TABLES OF IN SITU SNOW AND ICE MEASUREMENTS.....</b>	<b>54</b>

## INTRODUCTION

The Nansen Environmental and Remote Sensing Center in collaboration with partners organized a scientific cruise with the Norwegian Coast Guard's icebreaker KV Svalbard from 5 to 18 June 2021. The cruise included a research school for Master and PhD students with focus on practical training in use of various instruments for sea ice and ocean observations. The cruise took place in the sea ice area north of Svalbard and offered a unique opportunity to learn about field work and data collection in oceanography, ocean acoustics and sea ice research. The participants were really an international team of younger as well as more experienced researchers. The team consisted of 7 instructors and 12 students from 9 different countries: Norway, Poland, USA, Germany, Denmark, Russia, Canada, United Kingdom, and Turkey.

The cruise departed from Tromsø on 5 June and sailed to Longyearbyen to pick up equipment and personnel. The field work started with the deployment of an acoustic buoy on the first day when KV Svalbard entered the sea ice just north of Svalbard. The buoy recorded ambient noise data during the cruise and was received after one week on the way back to Longyearbyen. A part of the programme was the two-day long ice station where the students worked on the ice, learning how to use a number of different instruments for data collection. The work included drilling cores to measure sea ice thickness, snow cover and other properties. Drones were flown to obtain high-resolution images of the sea ice. An ROV with camera was used to observe the underside of the ice where ice algae were detected in many places. A 3-D scanning laser was used to map ridges in very high resolution. Satellite remote sensing data were obtained from Sentinel-1 and Radarsat 2 for mapping sea ice on regional scale and for planning the location of the ice station. The SAR data obtained every day in near real-time were important for use ice navigation to ensure that KV Svalbard could find the best sailing route through the sea ice. The oceanographic programme consisted of CTD-stations, XBT-casts, recovery and deployment of a bottom-anchored mooring under the sea ice. Work with moorings in sea ice is a challenging task, but the crew on KV Svalbard has built up long experience in such operations. Drifting buoys for the International Arctic Buoy Program were also deployed on ice floes in different positions during the cruise. The activities onboard the icebreaker and on the ice station was documented on video and will be part of the education and outreach material after the cruise. Before the cruise was completed and the participants went ashore in Longyearbyen all the data were assembled and organized on a hard disk for later processing and analysis.

After 14 days onboard KV Svalbard, the researchers and students disembarked in Longyearbyen, with an extensive dataset to investigate and lifelong memories of conducting field work on top of the Arctic Ocean.

### WHAT WAS THE AIM OF THE RESEARCH SCHOOL?

The research school provided training in use of instrumentation for data collection in oceanography, ocean acoustics, and sea ice research. Lectures about the Arctic ice-ocean environment and operations in the Arctic were given onboard by the scientists and KV Svalbard officers. After learning how to collect and document data in the field the students produced four videos about the activities during the cruise. These are available on YouTube (see <https://uak.nersc.no/summer2021> ).

### PROJECTS AND PARTIES THAT MADE THE RESEARCH SCHOOL ONBOARD KV SVALBARD POSSIBLE

The research school was part of the H2020 project *INTAROS–Integrated Arctic Observation System*, contract no 727890 (<http://intaros.eu>, <http://intaros.nersc.no>) and the project *Useful Arctic Knowledge*: partnership for research and education (UAK), funded by the Research Council of Norway contract no 274891). The research school was also supported by the project Digital Arctic Shipping, funded by the Research Council of Norway (contract no. 309708) for the drone work conducted by NORCE. Furthermore, Norwegian Meteorological Institute's Ice Service contributed with personnel and SAR data and the CIRFA project at University of Tromsø contributed with Fine-resolution Quad-pol SAT data. Office of Naval Research Global contributed with personnel and travel support. Finally, the Norwegian Coast Guard is

acknowledged for providing 14 days of ship time with KV Svalbard, which made it possible to organize the research school.



Figure 1. Group photo of the instructors and young scientists participated in the UAK 2021 research school. Photo by Hanne Sagen.



Figure 2. Bringing the equipment out on the ice for in situ measurements of snow and ice.

## 1. IN SITU SNOW AND ICE MEASUREMENTS

Authors: Jozef Rusin, Elinor Tessin

Instructors: Stein Sandven, Espen Storheim

A main goal of this activity is to learn how to collect data on sea ice physical properties (thickness, temperature, freeboard, salinity, density, snowcover and ridges) by working from an ice floe and use different instruments. These data are important for sea ice research and climate research because sea ice is very sensitive to climate change. The data will also be used for validation studies of satellite remote sensing and drone data in the same area, as described in section 3.

## 1.1. RESEARCH AREA

The in-situ work discussed in this chapter was done at ice station 1. This station was visited on the 11. and 12.06.2021 (reference point: 0847 UTC Lat: 81° 24' 29.24", Long 022°, 12' 27.05").

## 1.2. METHODS

Ice floe characteristics were studied through digging of snow pits, thickness drilling and ice coring. Characteristics such as snow and ice thickness, freeboard, temperature, density and salinity were recorded.

### 1.2.1. Snow pits

Snow pits were dug on various locations on a grid. Snow layers were visually identified. Total depth of the snow and depths of individual layers were then recorded. Temperature and density profiles were measured.

### 1.2.2. Thickness drillings

Snow thickness, ice thickness and freeboard were determined by drilling through the ice floe at various locations on a grid. Additional drillings were performed at the ROV transect and a ridge.

### 1.2.3. Ice coring

Ice cores were taken using a handheld battery drill with an ice coring barrel and shortened to 10cm when necessary. The length and weight of each core as well as temperature profiles were recorded. After melting the cores, conductivity was measured using a RBR Concerto CTD and a Hanna instruments DiST 2 tester.

## 1.3. RESULTS

The location of the eight snow pits where snow depth, freeboard, temperature and density was measured is shown in Fig. 1.1 and the measurements are plotted in Fig. 1.2. The tables of all the measurements are presented in in Appendix 2 (Table 1.1, 1.2. 1.3 and 1.4).

### 1.3.1. Snow pits

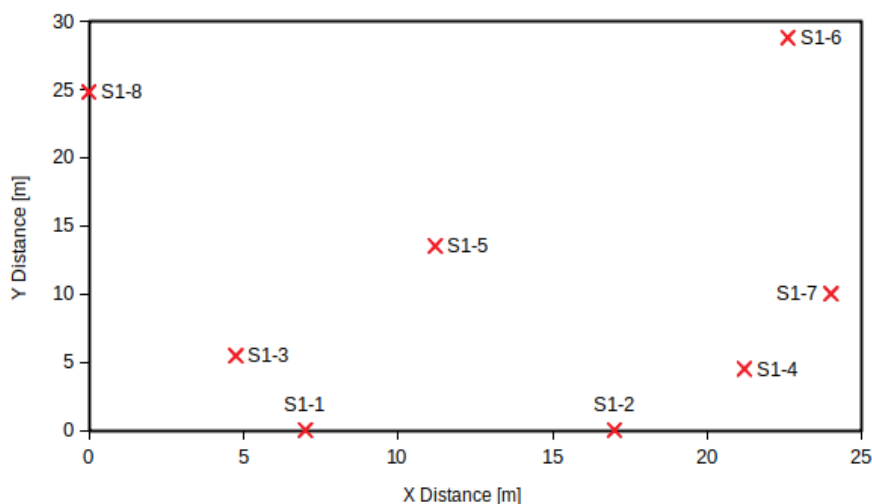


Figure 1.1: Snow pit locations. X-Y coordinates measured in meters relative to 0,0 axis which had a geolocation of 0842Z 81N24.501 022E12.495 on the 11th of June 2021.

### 1.3.2. Thickness drillings

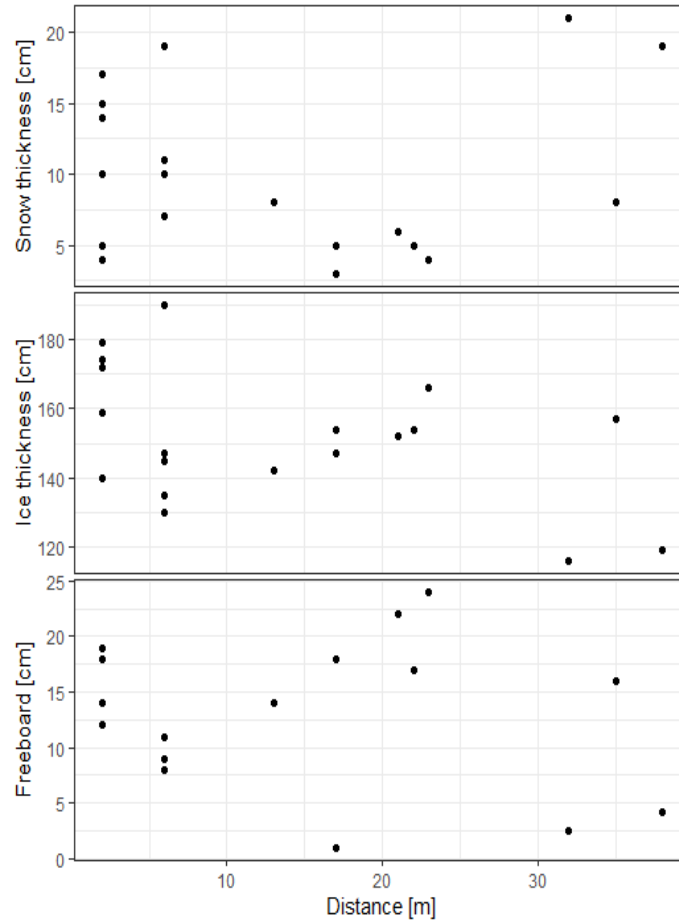


Figure 1.2: Snow thickness, ice thickness and freeboard from the points shown in Fig. 1.

### 1.3.3. Ice cores

A total of six ice cores were collected where profiles of temperature, salinity and density were measured. The results are plotted in Figs. 1.3, 1.4 and 1.5. All the profile data are also presented in Appendix 2 (Table 1.5).

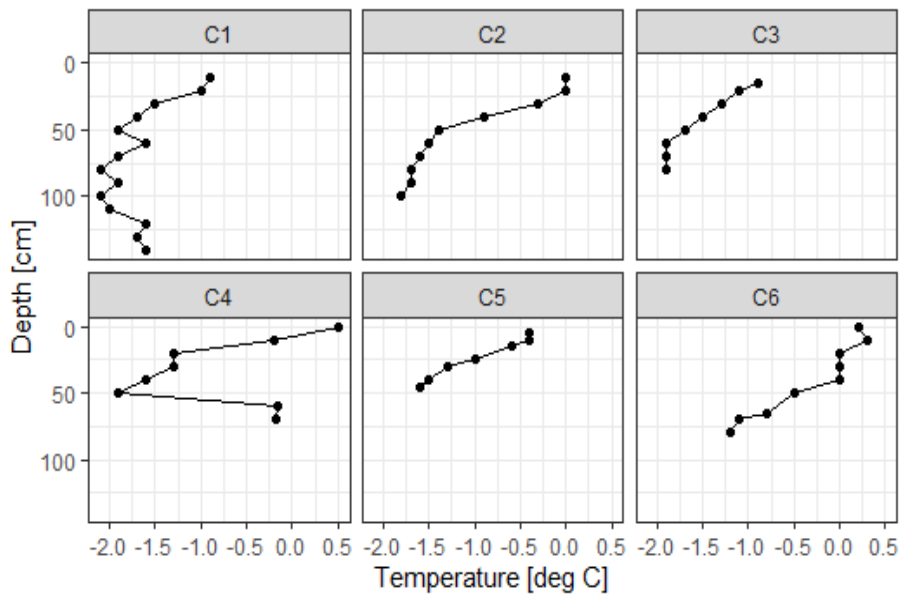


Figure 1.3: Temperature profiles of cores 1-6.

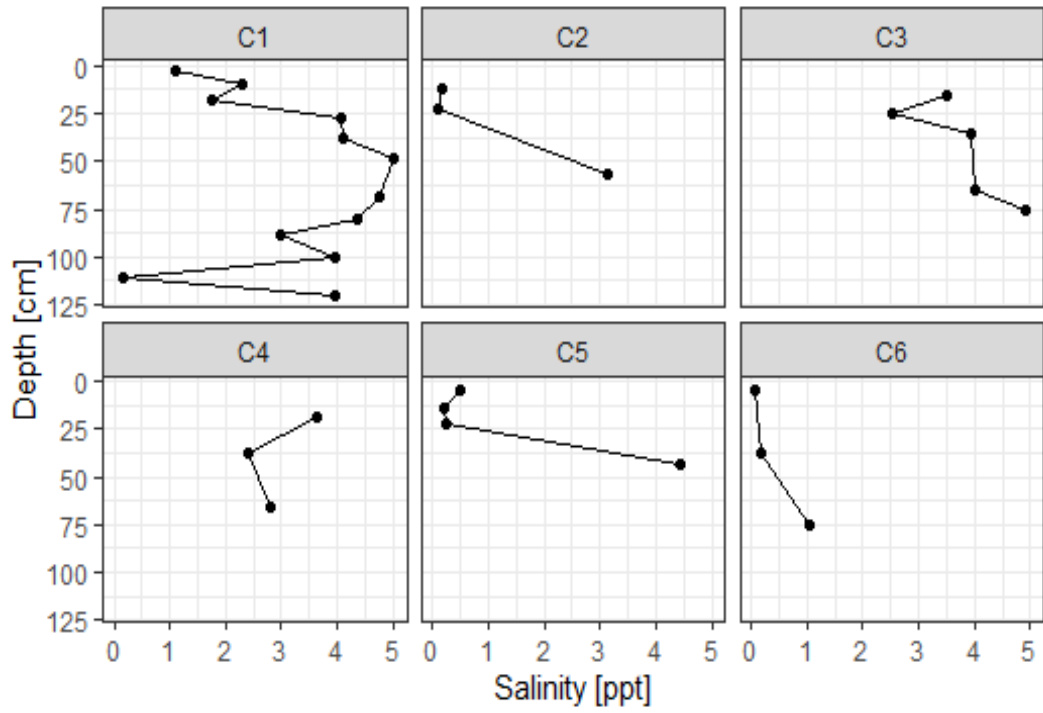


Figure 1.4: Salinity profiles of cores 1-6.

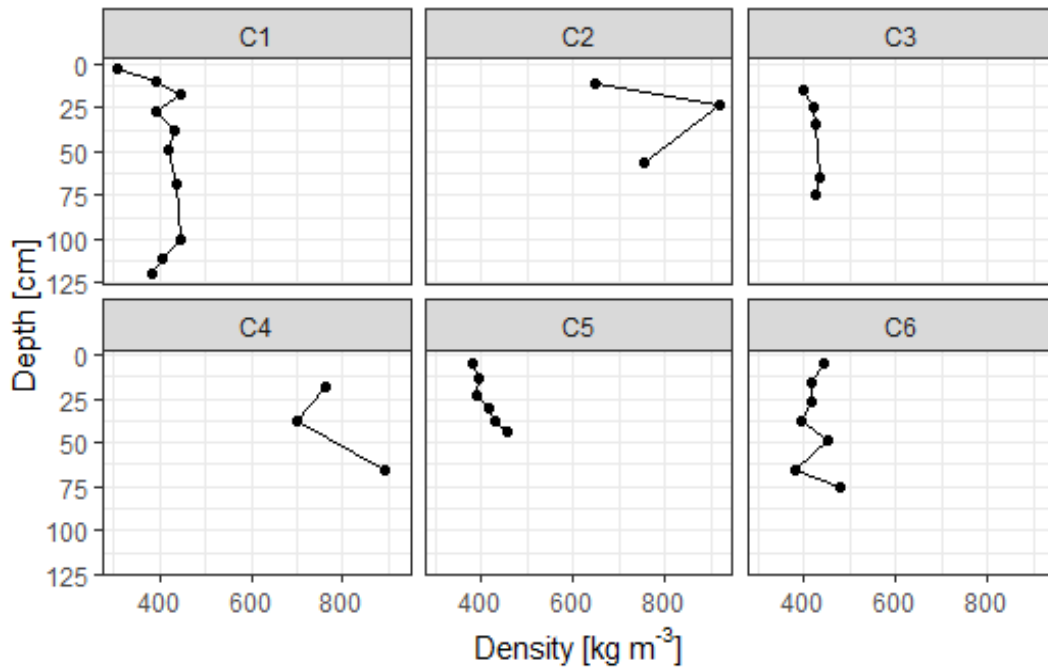


Figure 1.5: Density profiles of cores 1-6.

## 2. ROV WORK UNDER THE ICE

Author: Laust Færch

### 2.1. FIFISH 6V ROV

Viewing the ice from underneath, helps researchers understand the geophysical and biological processes occurring under the ice. On previous cruises, commercial *action cameras*, such as GoPro, were mounted on long poles and put through the ice. By slowly turning the pole, the camera could capture 360 degrees videos and images of the ice bottom. This method does not require a lot of resources, as holes already drilled for ice thickness measurements can be reused for the camera. But the cameras used typically do not provide a live feed from under the water, and the camera needs to be disassembled and the data uploaded to a computer before the video can be seen. This, of course, makes improvisation difficult, as interesting features are not spotted until after the camera is removed.

ROVs (Remotely Operated Vehicles) have been used in the past by researchers to collect data from underneath the sea ice. An ROV is a tethered underwater vehicle, which is remote-controlled by a pilot at the surface. ROVs are typically large, expensive machines operated by professionals, but small commercial drones/ROVs for hobby enthusiasts are also available on the market.

As part of the UAK cruise 2021, we wanted to test how small, commercial hobby ROVs could be used for mapping the bottom of the Arctic sea ice (Fig. 2.1).



Figure 2.1: ROV on the ice next to the deployment hole.

There are several advantages of using an ROV instead of an action camera. The ROV is completely mobile and often provides a live video feed, meaning that the pilot can control the camera and focus on interesting features. In that sense, the ROV can extend the point measurements that the action camera provides.

The purpose of this task was to test the possibility of using small, commercial ROVs for mapping the bottom of the ice. Before the cruise started, our initial plan was to acquire a series of images along the edge of a lead, with the purpose of creating a 3D map of the edge. However, as none of the ice stations had a suitable lead, this idea was scratched, and instead, we planned to map the underside of a ridge.

## 2.2. ROV OPERATION

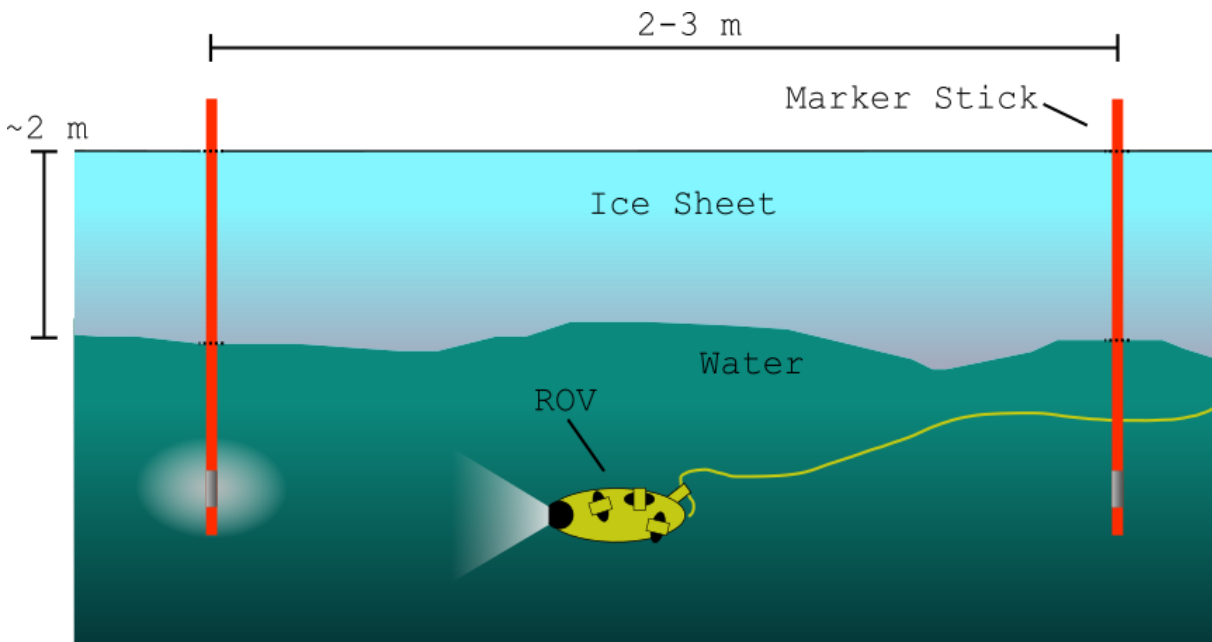


Figure 2.2: Diagram of the ROV and markers at ice station 2

The ROV used for the mission was borrowed by the department of drone technology at UiT and was of the type FIFISH 6V. This ROV costs around 1500 EUR and weighs around 4kgs. It contains a camera and two LED lights but does not have useful navigational sensors and must be operated by video only. The ROV can operate down to around 100 meters depth and is connected to the surface by a tether. The tether is connected to a controller, which in turn is connected via a wireless connection to a phone or tablet, on which the live video feed can be seen.

We deployed the ROV at two locations, ice station 1, and ice station 2. The deployment at ice station 1 was fairly short, with the main purpose of the deployment was to test the ROV under the ice. Even with very high visibility (above 5 meters), we quickly learned that navigating under the ice was very difficult due to the lack of distinct features. To solve this issue at ice station 2, we drilled a series of small holes along a transect, in which long red poles with reflective tape were attached. These poles could then be seen by the ROV, and greatly improved our ability to navigate (Fig. 2.2 and 2.3). The ROV was operated by a team of two people. One is responsible for controlling the ROV (the pilot), and the other being responsible for the tether.

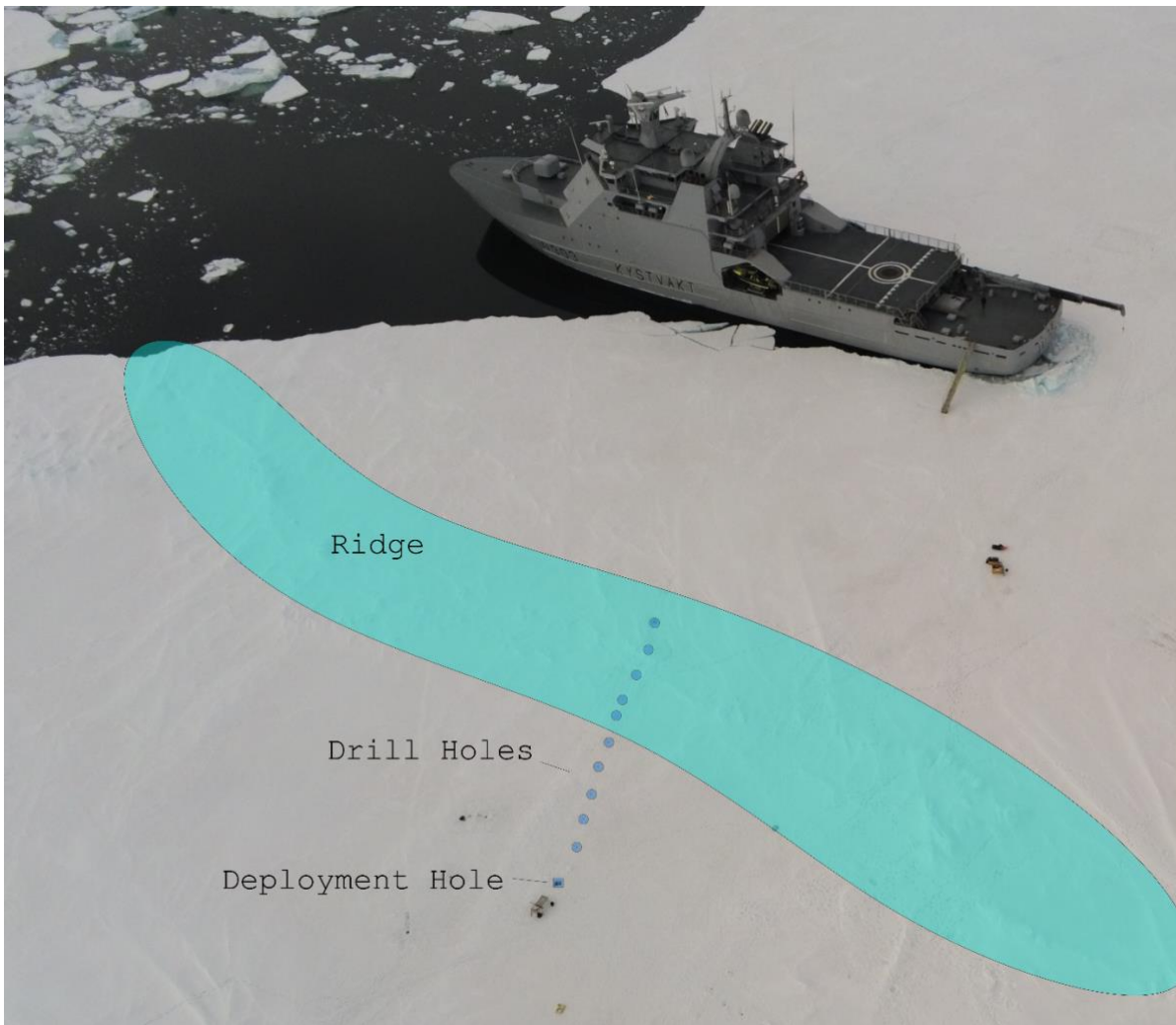


Figure 2.3: Overview of ice station 2

## 2.3.RESULTS

At ice station 1, the ice thickness was around 0.5 meters. This made the deployment easy, as we could manually cut a hole in the ice large enough for the ROV. The visibility at ice station 1 was very good, estimated to be above 5 meters. This meant that we could easily navigate 5 meters away from the deployment hole and find our way back again. But due to the lack of any distinct features of the sea ice, it was difficult to navigate any further away without a risk of getting lost. The bottom of the ice was fairly smooth with small cavities, probably because the sea ice was melting from underneath (Fig. 2.4)

We also noted a large amount of biological activity, as some sort of algae or seaweed was stuck underneath the ice. Additionally, we managed to film several jellyfish, possibly of the species *Mertensia Ovum* (Fig. 2.5).



Figure 2.4: The ice underneath ice station 1. Great visibility and plenty of seaweed

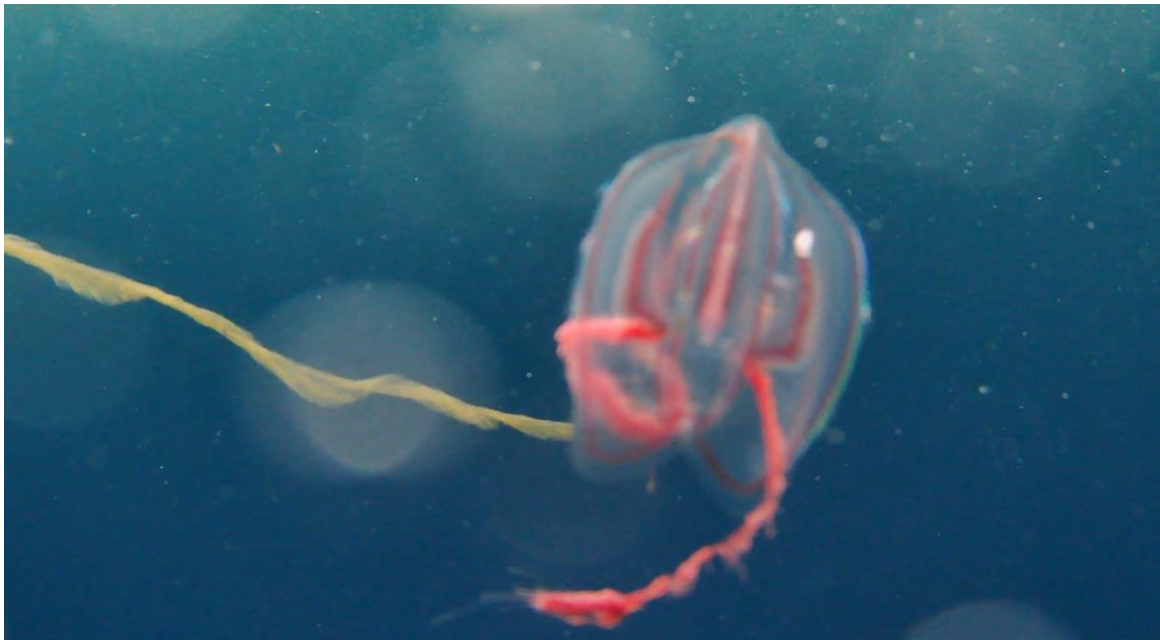
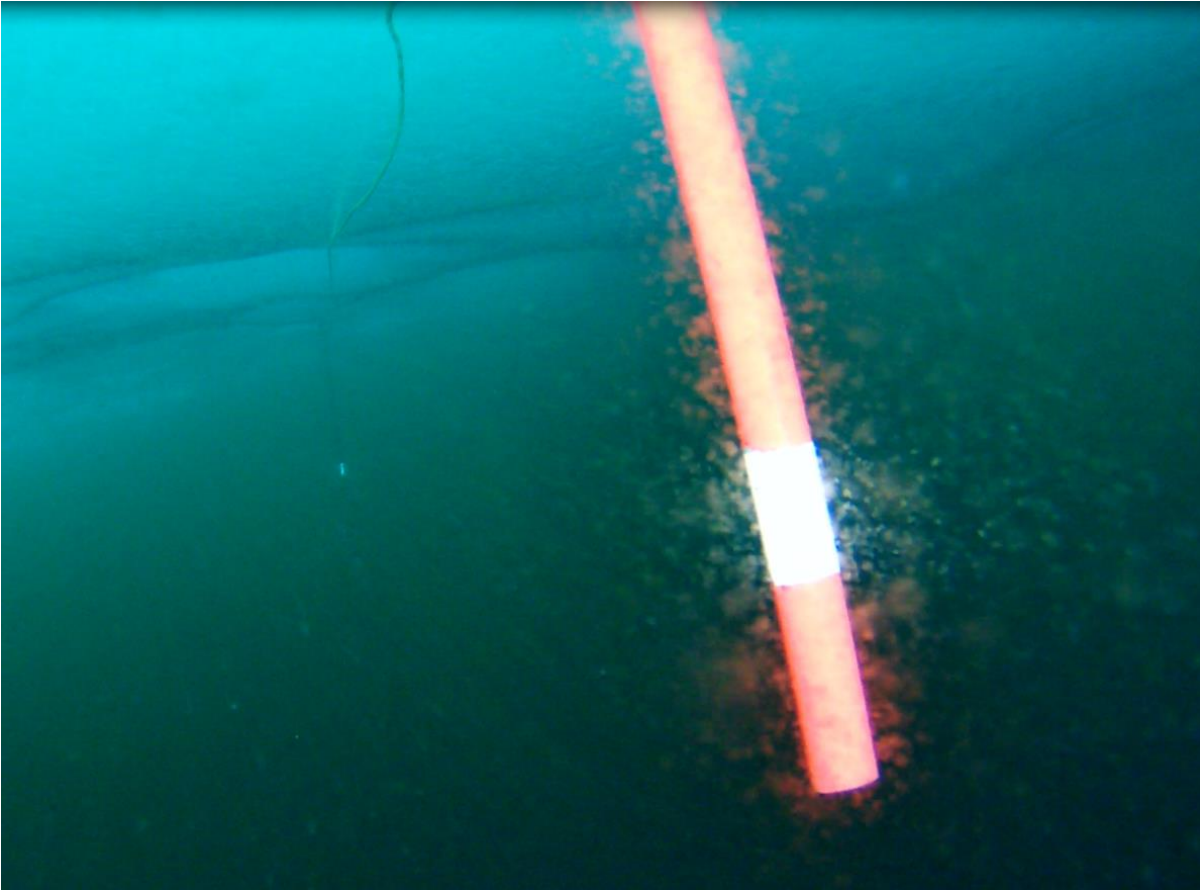


Figure 2.5: ROV image showing a jelly fish captured at ice station 1. Possibly of the species *Mertensia Ovum*.

The water at ice station 2 was much murkier with bad visibility. We estimate the visibility to be below 3 meters. Navigating the ROV proved very difficult, even with the reflector sticks. Reflector sticks were placed at 2-3 meter intervals. This was just enough to see the next reflector stick on the transect when using the ROV light (Fig. 2.6.)

At ice station 2, we completed a total of 3 dives. 1 test dive, and two dives along the entire transect of approximately 30 meters. The transect was made so it went underneath a ridge near the ship that could be identified from the surface (Fig. 2.3). Unfortunately, the ridge was almost completely featureless underneath the water. The lack of features, combined with the low visibility, meant that the data is ill-suited for 3D mapping.



*Figure 2.6: Ice station 2. ROV image showing two reflector sticks. Visibility around 2-3 meters.*

## **2.4. ISSUES**

Our experience with the ROV revealed a series of issues which are outlined below.

### **2.4.1. DIFFICULT CONTROL**

By far the biggest issue during the operation was the difficulties that occurred when controlling the ROV. This was in part, due to the inexperience of the pilot (me), but also due to system/software issues. At the time, the ROV would run amok, e.g., without any input from the operator, it would start rotating, turning, or driving to the side. We also experienced that the controls inverted mid-dive. The ROV was controlled using the USA-UAV configuration, but the controls would at times suddenly change so up/down was forward/back. It was always possible to regain control by switching the ASC button on the left on and off. However, if the ROV is being operated in a more demanding environment, these errors could become critical.

### **2.4.2. APP INTERFACE UNITS**

Changing the units (e.g., feet/meters and Fahrenheit/Celsius) using the App interface did not work. This issue was persistent meaning all images and video recorded had a Fahrenheit/Feet watermark even though we wanted SI units.

### **2.4.3. DATES AND TIMESTAMPS**

For a few of the videos, the timestamp saved with the video was not matching the time on the iPad used. This also meant that the timestamp watermark on videos was wrong. This issue only occurred a few times and did not seem to have anything to do with the time on the iPad.

### **2.4.4. BEEPING SOUNDS**

Two times the ROV started beeping while exporting data to the SD card. This did not appear to have anything to do with a low power level. Inspection of the documentation did not reveal why the beeping sound was supposed to notify.

### **2.4.5. DATA EXPORT**

One video was corrupted when exporting data to the internal SD card. The issue was solved by exporting the data directly to a phone over WIFI instead.

### **2.4.6. CLIPPING OF VIDEOS**

Long videos were clipped to several shorter videos of a max 3-minute length (~1.1 GB) when exporting. This happened when exporting to the SD card. The issue could be caused by the SD card, but we did not have a spare SD card for testing.

### **2.4.7. CAPTURING PHOTOS**

The ROV control unit had a button for capturing photos. However, this feature did not always work. Sometimes when pressing the button, the App would change from image mode to video mode instead of capturing an image. Images could be captured by pressing the button of the App instead.

Several of the issues outlined above seems to indicate some sort of software or device error. None of the issues occurred during testing of the ROV before the cruise (in an in-door swimming pool). However, the ROV was operated using another iPad than the one used for testing. The iPad used on the ice was a slightly older model, and we speculate if switching to a newer iPad could have resolved some of the issues.

## **2.5.FINAL REMARKS**

The ROV worked remarkably well in the cold weather, and there is a lot of potential in using similar equipment on future cruises. At ice station 2, the ROV ran for around 2 hours, with the lights turned on, in water temperatures just above freezing.

Our main issue was navigation and control of the ROV. The navigation was made difficult due to low visibility and the lack of features under the sea ice. This restricted us to operate near the deployment hole, and along a predefined transect on which a series of sticks visible under the ice was mounted. The navigation sticks greatly improved our ability to operate in low visibility. But also created a risk of entanglement.

As we had chosen a transect running below a ridge, we expected the underside of the ice to be rich in features, this, unfortunately, proved not to be the case. Later inspection of another area around 100 meters from the deployment hole near another ridge, showed a rich ice landscape with large pieces of ice going down several meters into the water. If we had scouted several areas with the action camera before deciding where to cut the deployment hole, we would have been able to find a more suitable location for deploying the ROV. Additionally, having more days at the ice station would have enabled us to choose a time with better visibility. This would have made it easier to navigate the drone, and thus made it possible to cover a larger area.

Cleaning the ROV after operation requires leftover power on the battery. As the battery was very low after operating under ice station 2 for 2 hours, there was not enough battery for running the maintenance cleaning program. This was solved by lowering the ROV into a plastic box with lukewarm water. As the temperature of the ROV rose, so did the battery level, and after a few minutes, the maintenance program could be executed.

Even though the ROV could be operated by a single person, it is recommended to operate in a two-person team. While the pilot is responsible for controlling the ROV, the helper makes sure that the tether is not too tight or too loose. We experienced several times how too much tether in the water, creating a risk of getting entangled in the tether (Fig. 2.7).

For best control of the ROV, it is recommended that the pilot is shielded from snow and sunlight. For new missions, we recommend acquiring a small tent, possibly of the type used for ice fishing. This would also keep the people safe from wind and snow.

Cutting a hole to deploy the ROV was done manually. At ice station 2, the ice thickness was around 2 meters and cutting a hole large enough for the ROV took several very work-intensive hours.

As plastic becomes very brittle in cold weather, it is recommended to store the ROV somewhere warm when not deployed into the water. As we operated the ROV in June, the weather was relatively warm, with air temperatures above freezing, but this might not be the case on future cruises.

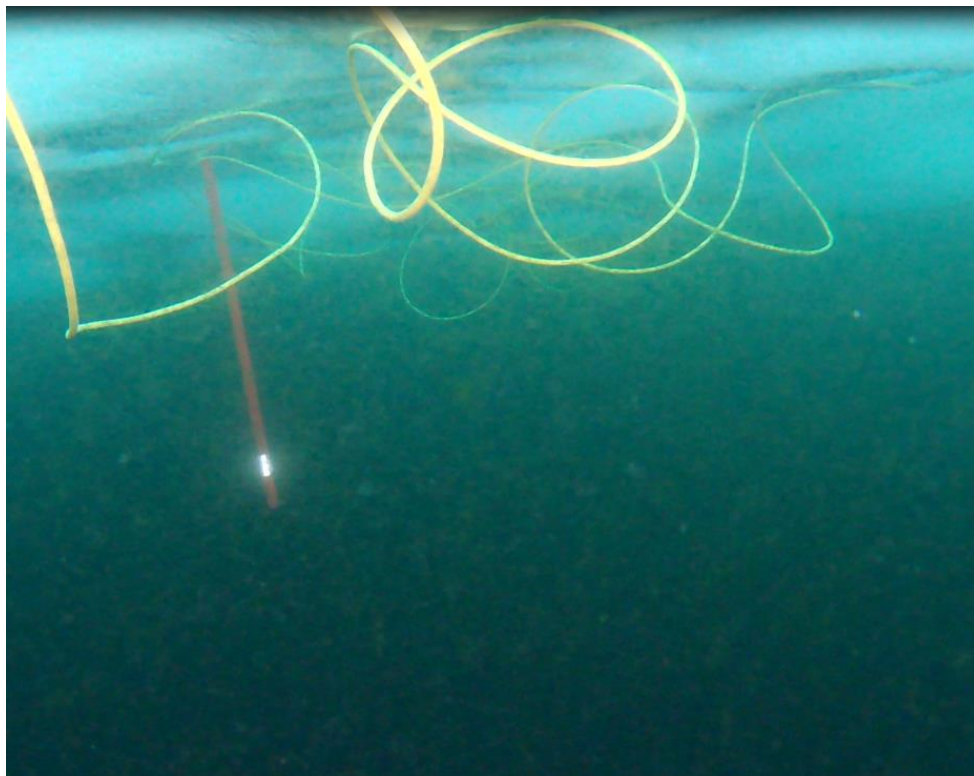


*Figure 2.7: Ice station 2. If the tether is not well managed, the ROV is in risk of being caught in the leftover tether.*

### **3. SEA ICE REMOTE SENSING AND IN SITU VALIDATION DATA**

Authors: Laust Færch, Jozef Rusin, Anna Telegina, Elinor Tessin

Instructors: Alistair Everett, Tom Rune Lauknes

Part of the work performed by the UAK participants (students and instructors) has been published

<https://blogs.egu.eu/divisions/cr/2021/09/10/mapping-sea-ice-from-space/>

### 3.1. INTRODUCTION

As well as being an essential component to the global climatic system, sea ice also has a significant impact on navigation and offshore activities in polar regions. Being able to map the sea ice and classify the types of sea ice present will ensure safety, sustainable economic activities, and greater scientific insight (Zakhvatkina et al., 2019).

The sea ice type present is dependent upon the development stage and the meteorological, atmospheric, and other physical conditions present. Generally, as the ocean begins to freeze, needle-like ice crystals form which then accumulated at the surface, bonding together to create sheets of ice. If growth is sufficient through winter, it will not completely melt in the following melt season. It can then continue to grow and thicken the following winter; this is referred to as old ice. Each stage of the sea ice formation is defined in Table 3.1.

Table 3.1. Sea ice types based on stage of development (adapted from Shokr & Sinha, 2015)

Stages of Development	Subtype	Definition	Dimensions
New ice	Frazil	Fine spicules suspended in water.	
	Grease	Crystals coagulated to form a soupy layer. Reflects little light.	
	Slush	Snow mixed with water on ice surface after heavy snowfall.	
	Shuga	Accumulation of spongy white ice lumps formed from grease ice.	A few cm's across.
Nilas	Dark Nilas	Elastic crust, very dark in colour.	<5 mm thick
	Light Nilas	Elastic crust, lighter in colour.	>5 mm thick
Young ice	Gray	Less elastic than Nilas. Breaks on swell. Usually rafts under pressure.	0.1–0.15m thick
	Gray-White	Under pressure, it is more likely to ridge than to raft.	0.15–0.3 m thick
First-year ice (FYI)	Thin FYI	Sea ice of not more than one winter's growth, developing from young ice.	0.3–0.7 m thick
	Medium FYI		0.7–1.2 m thick
	Thick FYI		>1.2 m thick
Old Ice	Second-year Ice (SYI)	Ice survived one summer's melt; it stands higher out of the water.	
	Multiyear Ice (MYI)	Ice survived more than one summer's melt. Hummocks are smoother than SYI ice.	

Each ice type has its distinctive characteristics but within each subtype appearance may vary greatly. A main source of this diversity is deformation, which is also a key factor considered in sea ice navigation. Hummocked and ridged ice impedes navigation whilst fractured ice with cracks and leads are more favourable for ship routing. Operationally, remote sensing data are the main sources used to provide this sea ice information. Synthetic Aperture Radar (SAR) is used by national ice services to provide this data due to its high resolution, continuous imaging capabilities during the polar night, and its independence of cloud cover (Dierking, 2013).

SAR imagery provides a backscatter intensity of the radar reflections from the surface. The intensity is dependent on the radar frequency, polarisation, incidence angle and the dielectric properties of the ice (Dierking, 2013). Consequently, interpretation of SAR is challenging due to the ambiguities of sea ice backscatter (Zakhvatkina et al., 2019). Validation datasets are required for the development of ice-type algorithms to ensure robust and accurate scientific analysis of the sea ice conditions. The collection of ground truth data will provide greater information about the sea ice and its physical surroundings and enable the accurate determination of ice types. This can be used to provide contextual information when compared to remote sensing data to determine the accuracy or causes of misclassification. The objective of this fieldwork was to collect this validation data at two ice stations on two separate ice floes (Fig. 3.1).

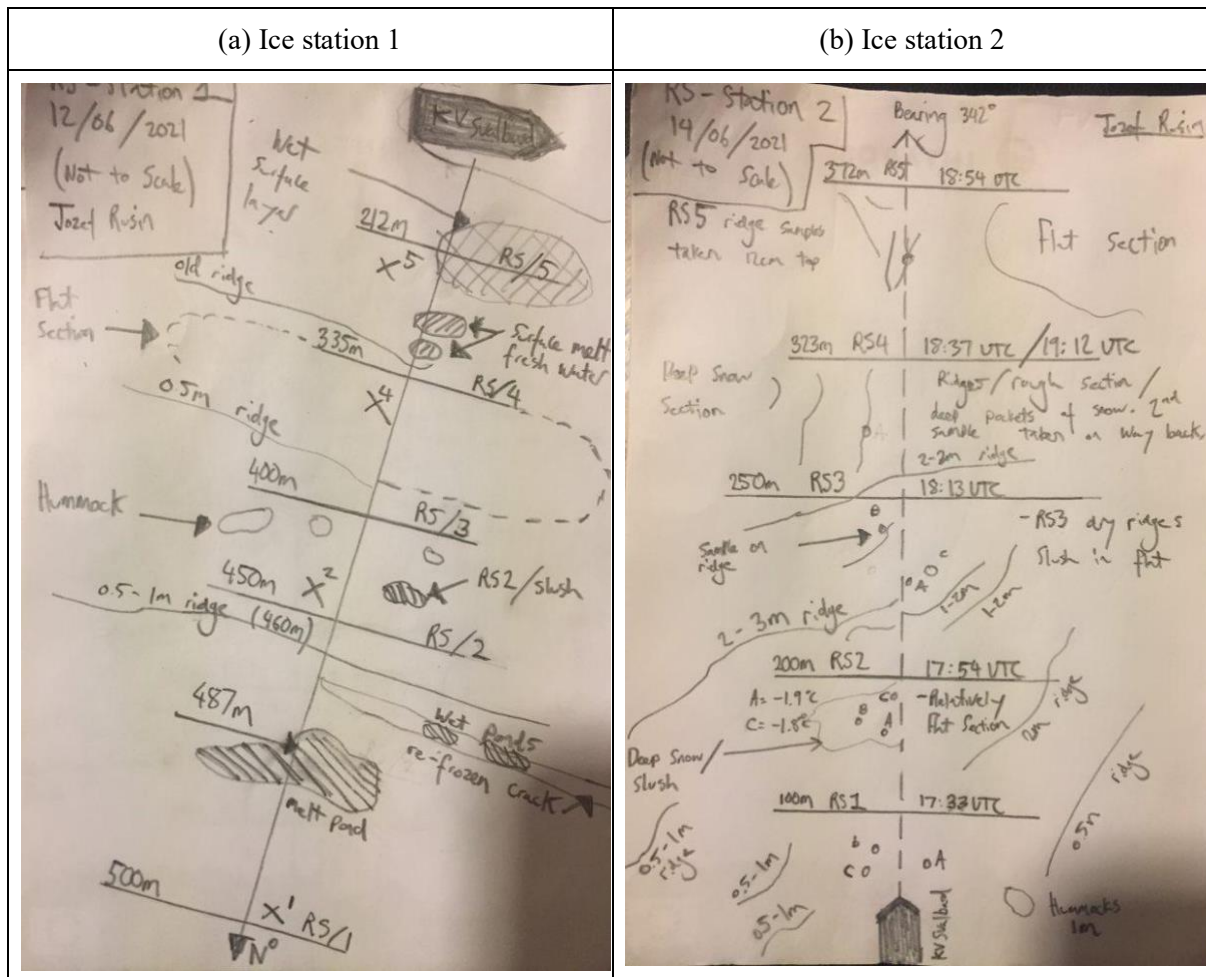


Figure 3.1. Field sketches of ice stations 1 & 2. At each ice station in situ sampling was undertaken along a ~500m transect (Table 3.2).

Table 3.2. Ice station transect overview

	Ice station 1	Ice station 2
Date	12/06/2021	14/06/2021
Start point (Lat/Lon)	81°26'0.959N, 22°30'0.003E	82°5'12.830N, 10°14'4.477E
End point (Lat/Lon)	81°25'54.839N, 22°30'34.263E	82°5'29.162N, 10°6'8.559E
Time of sampling (start & end)	12:15 to 13:31 UTC	17:35 to 18:56 UTC

## 3.2 METHODS

### 3.2.1 Sea ice classification based on SAR imagery

For sea ice type identification, the automatic classification used during the cruise was the Lohse, et al., 2020 algorithm, that was applied to Sentinel-1 and RADARSAT-2 imagery. This is a supervised classification algorithm that includes the surface-type dependent effects of the incidence angles in its classification.

Smooth surfaces such as new ice, nilas and level young ice are specular reflectors, reflecting the signal in the opposite direction from the source causing these ice types to appear dark in the image. With time ice experiences deformation creating rough surfaces increasing the backscatter creating a brighter appearance in the image. Brightness of the sea ice can also be determined by volume scattering when the radar signal penetrates deeper into the surface layer. This occurs in older ice since the salinity (especially in the upper layers) is lower due to brine rejection. This creates pores in the ice which increase the scattering making MYI appear bright in SAR images. These processes described are relatively consistent during the winter under cold conditions. During melting season, sea ice differentiation becomes more challenging due to melt water on the surface decreasing the contrast in the SAR image.

The algorithm was run on Sentinel-1 and RADARSAT-2 images for ice station 1 and only Sentinel-1 for ice station 2. The spatial resolution of Sentinel-1 (93x87m, range x azimuth) is lower compared to RADARSAT-2 (9-30x7.6m). However, Sentinel-1 covers a greater AOI due to having a larger swath width of 400x400km compared to the 30x30km of RADARSAT-2.

Due to the SAR spatial resolution and ambiguities present for certain sea ice types, classification methods often do not differentiate between subtypes of sea ice (Table 3.1), specialising only in general types. Furthermore, the classification output contains additional ice types not defined in the traditional World Meteorological Organization nomenclature (Armstrong, 1972). For example, FYI is often split into level and deformed ice type which is beneficial for ship routing. The classified image obtained during the expedition covered following sea ice types:

- Open water (windy)
- Leads with open water/newly formed ice
- Young ice
- Level first year ice
- Deformed first year ice
- Second year ice

Since the cruise was taking place in June, melting processes had already begun effecting the SAR signal. The task of the remote sensing group was to evaluate how representative the classification's results are in the summer season and what physical sea ice processes could be influencing the classification.

### 3.2.2 Field Data

Snow depth and structure, presence or absence of water, ice salinity and ice density were collected to understand the surface characteristics. Sampling was performed at five sampling sites along each transect. Transects were selected to cover as many different ice types and features classified in the SAR imagery as possible. Samples were taken at features of interest along the transect (Figure 3.1a & b). The distances were measured with a ranging device. At ice station 1, the aim was to recover one ice core and one snow profile for each site. At ice station 2, three ice cores and one snow profile per site was collected. If slush was present, a sample was collected and if possible, a core from underneath.

Table 3.3. Ice station 1 & 2, sample sites 1-5 with GPS coordinates, distance from ship and site descriptions.

Ice station 1			
Site	GPS coordinates	Distance from ship [m]	Site description
RS1	81°26'0.95912N, 22°30'0.00348E	500	Fairly flat, 1m hummocks present.
RS2	81°26'0.31396N, 22°30'10.63252E	450	Old Ridges present surrounding site.
RS3	81°25'59.34758N, 22°30'19.96605E	404	Old Ridges present before flat area, 50cm to 1m ridges.
RS4	81°25'57.70465N, 22°30'25.6316E	335	Flat relatively homogenous area, no ridges, slight humps
RS5	81°25'54.83925N, 22°30'34.26326E	212	Flat uniform area, old ridges/ hummocks 30m east of sampling site.
Ice station 2			
RS1	82°5'12.82985N, 10°14'4.47729E	100	Fairly flat, some 0.5 - 1m ridges present surrounding site.
RS2	82°5'17.0906N, 10°11'55.72304E	200	Fairly flat section with deep snow.
RS3	82°5'20.26714N, 10°10'7.89898E	250	Flat. Slush present.
RS3	82°5'12.82985N, 10°14'4.47729E	250	2-3m dry ridges.
RS4	82°5'26.29535N, 10°6'59.27447E	323	Ridges and rough section with deep pockets of now. Second sample taken on return.
RS5	82°5'29.16218N, 10°6'8.55945E	372	Samples taken from ridge. Flat area nearby.

### 3.2.3 Ice coring

Ice cores were taken using a handheld battery drill with an ice coring barrel and shortened to 10cm when necessary. The length and weight of each core was recorded. At ice station 2, temperature at the top and bottom of each core were also taken. At slushy sites, the surface temperature of the slush was measured. After the cores melted, the conductivity samples were measured using a RBR Concerto CTD and a Hanna instruments DiST 2 conductivity tester. At ice station 2, only RBR Concerto was used.

### 3.2.4 Snow

Snow layers were visually identified from the snow pits created. Total depth and depths of the layering were then recorded. At ice station 2, air temperature and snow temperature at 5 cm intervals (10 cm when snow depth was >1 m) were also recorded.

## 3.3 RESULTS

This section is a record of the transect data collected and preliminary data visualisation.

Table 3.4. Ice station 1, salinity and weight of ice and slush samples, as well as snow thickness at each site.

Site	Ice salinity (DiST2) [ppt]	Ice salinity (RBR Concerto)[ppt]	Ice sample weight [g]	Snow thickness [cm]
RS1	0.50	0.36	640	16

RS2	4.60	5.06	630	54
RS2-Slush	8.57	11.02	/	/
RS3	5.30	5.88	620	50
RS4	0.04	0.03	610	22
RS5	0.03	0.02	630	16

Table 3.5. Ice station 2, snow thickness and air temperature measured at each site. RS5 snow thickness is provided as a range since significant variation was present between sample points.

Site	Snow thickness [cm]	Air temperature [°C]
RS1	26	-1.1
RS2	28	-1.0
RS3-Flat	21	-1.0
RS3-Ridge	83	-1.1
RS4	82	/
RS5	13-90	-0.6

Table 3.6. Ice station 2, length, depth, top and bottom temperature, and weight of ice samples taken at sites 1 - 5, as well as salinity of melted ice and slush samples.

Site	Core Sample	Core Length [cm]	Depth [cm]	Ice Core Temperature Top [°C]	Ice Core Temperature Bottom [°C]	Weight [g]	Salinity [ppt]	Comments
RS1	A	10.0	/	-3.6	-3.3	600	6.00	
RS1	B	15.0	/	-2.1	-2.0	920	0.70	
RS1	C	15.0	/	-2.1	-2.3	1050	4.70	
RS2	A	/	35	-1.9	-1.9	/	9.30	Slush
RS2	B	/	29	-1.8	-1.8	/	15.00	Slush
RS2	C	/	27	-1.8	-1.8	/	13.25	Slush
RS2	D	/	/	/	/	/	16.00	Slush
RS3	A	/	10	-1.9	-1.9	/	/	Slush
RS3	B	15.0	/	-1.8	-2.0	1000	1.95	Sample from ridge
RS3	C	/	10	-1.8	-1.8	/	16.40	Slush
RS4	A	10.0	/	-0.3	-0.5	650	0.06	Ridge, large grain snow
RS4	B	/	/	/	/	/	15.20	Flat area
RS5	A	12.0	/	-0.6	-0.7	780	1.34	
RS5	B	13.5	/	-0.8	-0.9	700	/	

### 3.3.1 Snow Height and Temperature

Snow height above the ice was highly variable along each transect, with a range from 16 to 54 cm at ice station 1 and 13 to 90 cm at ice station 2 (Tables 3.4 – 3.6, Fig. 3.2). At station 1, one snow depth measurement per site was taken. At station 2, the diversity of the terrain at each site was obtained by digging two snow pits at site RS3 and RS5. Resulting in two depth measurements for these sites (Fig. 3.2).

Snow temperature profiles (Fig. 3.3) were highly variable with depth, and ranged between 0.1 and  $-2.4^{\circ}\text{C}$ . At sampling sites RS1, RS2 and RS3-Flat, where snow height was similar, temperatures at the snow surface were also alike. Temperatures then increased with depth and then decreased again towards the ice interface. At sites RS3-Ridge and RS5, temperatures at the surface were higher and then decreased approximately linearly towards the ice interface. As air temperature (Table 3.5) increased slightly during the transect, this might account for higher surface temperatures at these later sites.

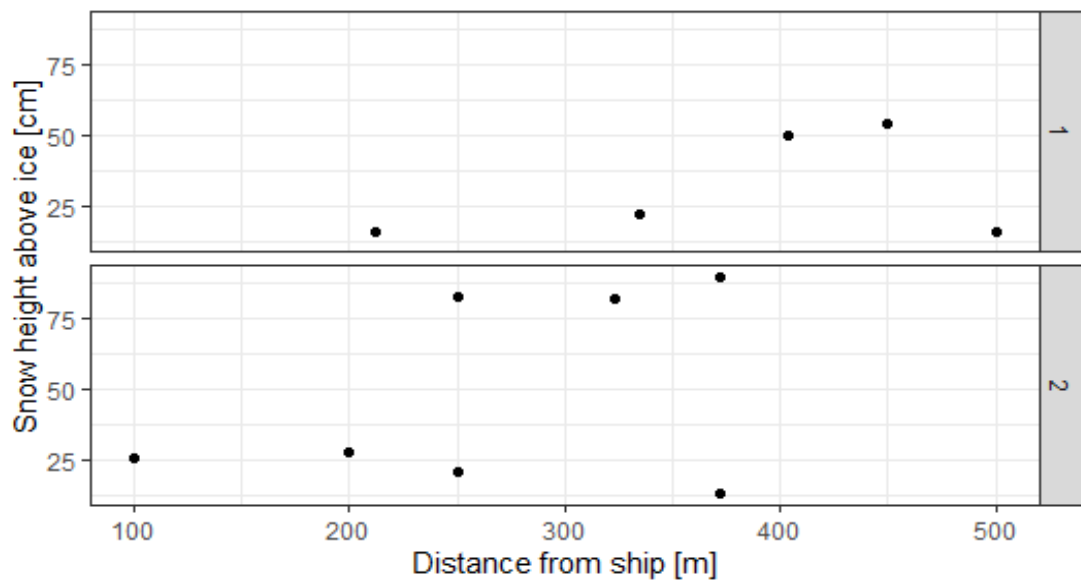


Figure 3.2. Snow height above ice on transects at ice stations 1 and 2. At station 2, two snow pits were dug at sites RS3 and RS5, resulting in two depth measurements for these sites.

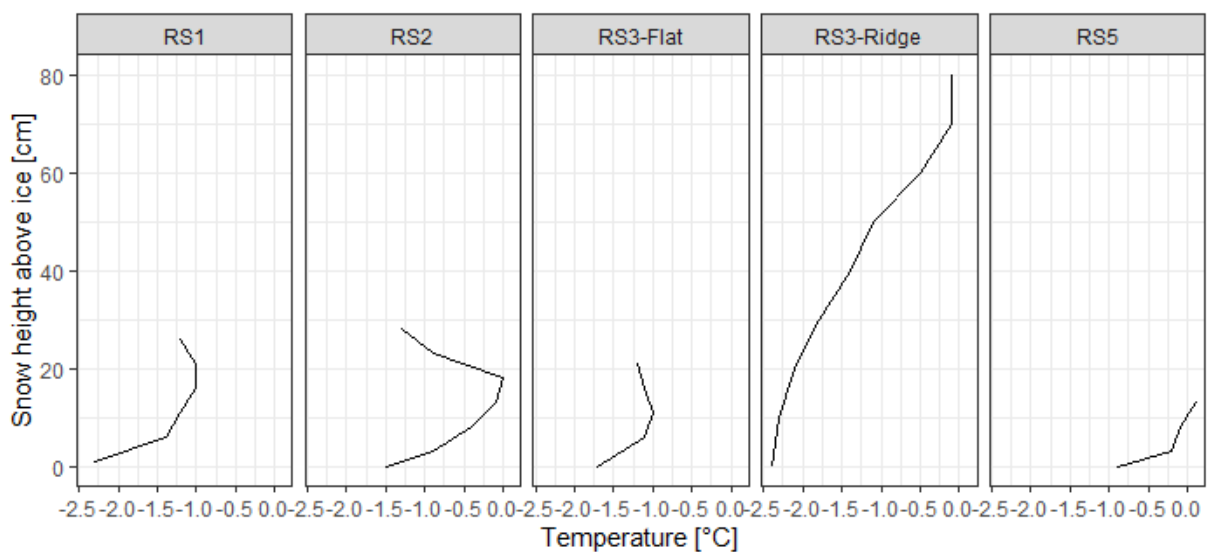


Figure 3.3. Snow temperature profiles of sites RS1-3 and RS5 at ice station 2.

### 3.3.2 Salinity

At ice station 1, one ice core was taken per site. At RS2 (450 m from the ship, Fig. 3.4), an additional slush sample was taken, which was higher in salinity than the solid ice sample. At Ice Station 2, multiple cores were collected at each site but due to time constraints this was reduced at the end of the transect. Initially samples at each site were taken close by causing minimal salinity variation (Fig. 3.4). At ice station 2 on sites RS3 and RS4, where the terrain was more heterogenous, samples were taken from the top of a ridge (RS3B, RS4-A) and a flat region (RS3C, RS4-B) (Table 3.6). Both ridge samples were lower in salinity than the samples taken from flat areas. Slush samples were generally saltier than solid samples.

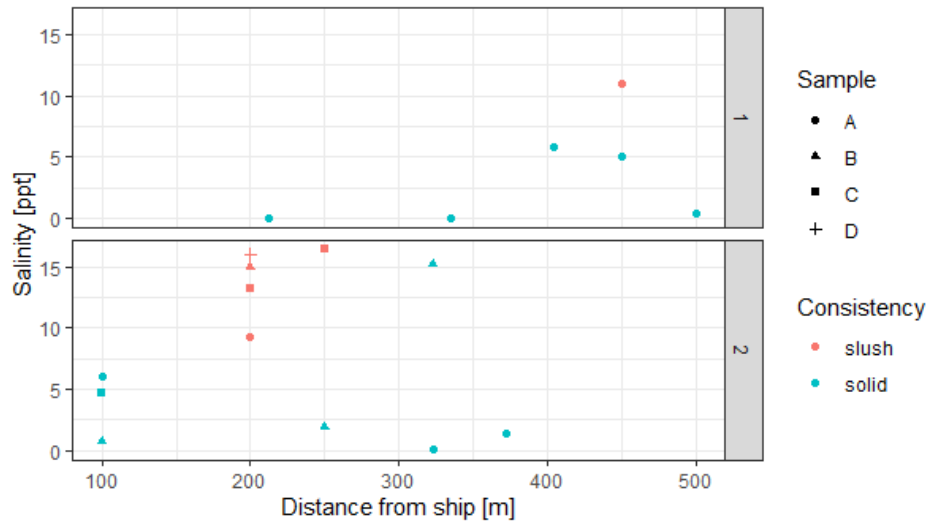


Figure 3.4. Salinity of ice and slush samples taken on transects at ice stations 1 and 2, measured with the RBRConcerto.

### 3.3.3 Ice Temperature

The top and bottom temperatures of ice cores were measured immediately after sampling (Fig. 3.4) to see if any significant variance was present. The temperatures ranged between  $-0.3$  to  $-3.6^{\circ}\text{C}$ , with little variation being present (Fig. 3.5).

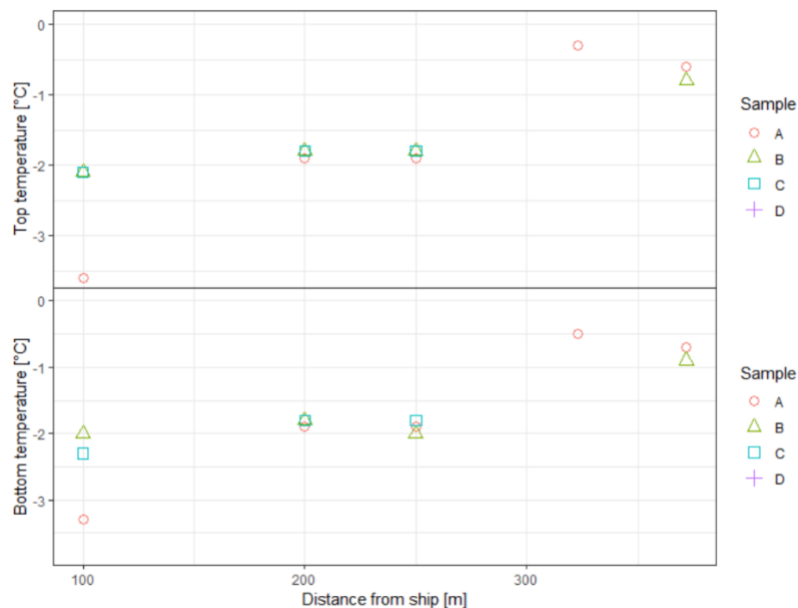


Figure 3.5. Temperatures measured at the top and bottom of each sampled ice core during the transect at ice station 2.

### 3.3.4 Classification

Since the classification strongly depends on the chosen settings and training procedure, a few variants of settings were used for Sentinel 1 images. Imagery from the 9<sup>th</sup> of June was chosen for the comparison instead of 12<sup>th</sup> despite it is preceding the corresponding fieldwork sampling. This was because ice station 1 in the image for 12<sup>th</sup> was located within the 1<sup>st</sup> swath of the SAR image which is unsuitable for the adequate classification (Lohse, Doulgeris & Dierking, 2020). Data were processed at 40x40m in the radar geometry and then geocoded to 200x200m which is approximately the same resolution after applying a 5x5 multi-looking.

RADARSAT-2 classification results corresponded to the 10<sup>th</sup> and 11<sup>th</sup> of June. The scenes were 2x2 multi-looked and resampled to 30x30m pixel size. The output for the 11<sup>th</sup> was chosen for the final comparison since it contained less misclassifications caused by windy conditions.

Based on the Sentinel-1 classification (top of the Fig. 3.6), FYI prevailed in June 2021 North of Svalbard without traces of MYI. Ice at the south part of the image is characterised by higher deformation levels since the prevailing ice type there is deformed FYI. From the SAR image (bottom of the Figure 6), this type of ice is characterised by brighter surface. It is important to note that high intensities might be caused by more factors than deformation of surface, that is why extra analysis is needed (see discussion chapter).

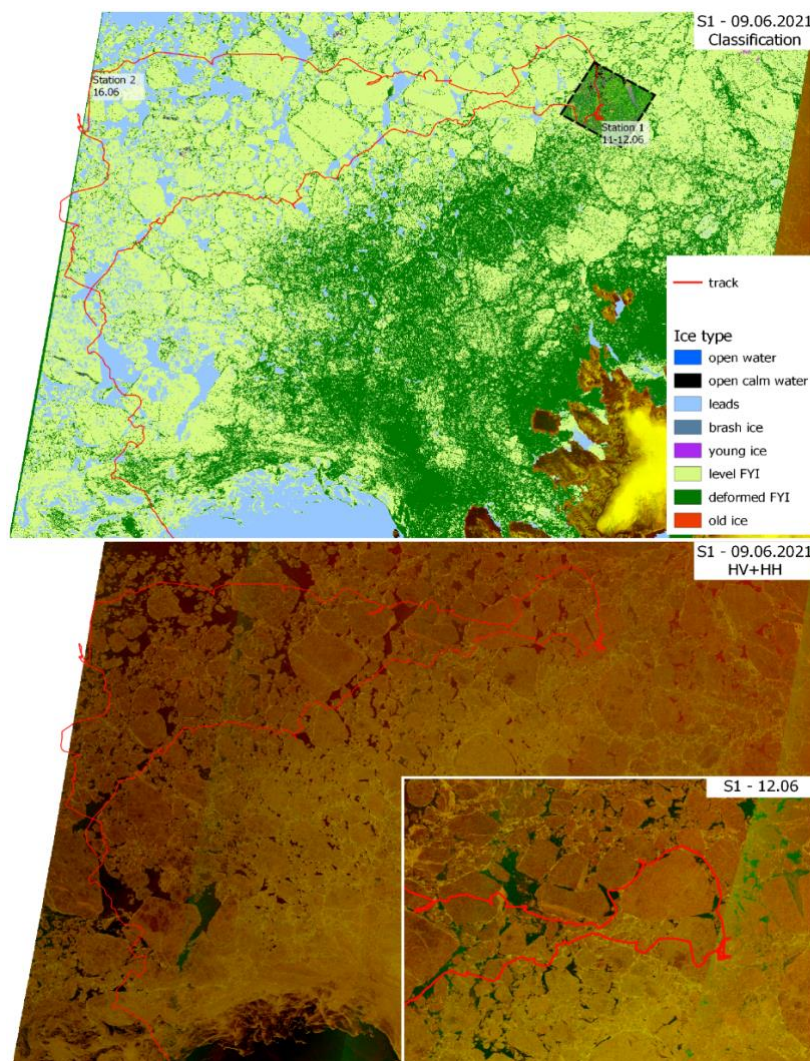


Figure 3.6. Example of the sea ice classification results for the Sentinel-1 EW and RADARSAT-2 Quad-Pol mode images (top). Sentinel-1 composite image in false colours (HH+HV) is presented at the bottom. The red line represents the track of the icebreaker. Due to sea ice drift, the track in relation to the sea ice is not accurate for the North-East of the image from 09/06/2021. The image from the 12<sup>th</sup> is more representative for the North-East.

### Ice station 1

The ice of ice station 1 was mainly characterised by deformed FYI according to the RADARSAT-2 classification results and level FYI according to the Sentinel-1 classification (Fig. 3.7). The ship radar data on the Fig. 3.8 shows that RADARSAT-2 sea ice type map provides realistic distribution of the ice types around the floe but possibly overestimates the level of deformation. The resolution of the Sentinel-1 sea ice map is too low for good representation of ice type distribution within a small floe. For better results higher resolution should be used.

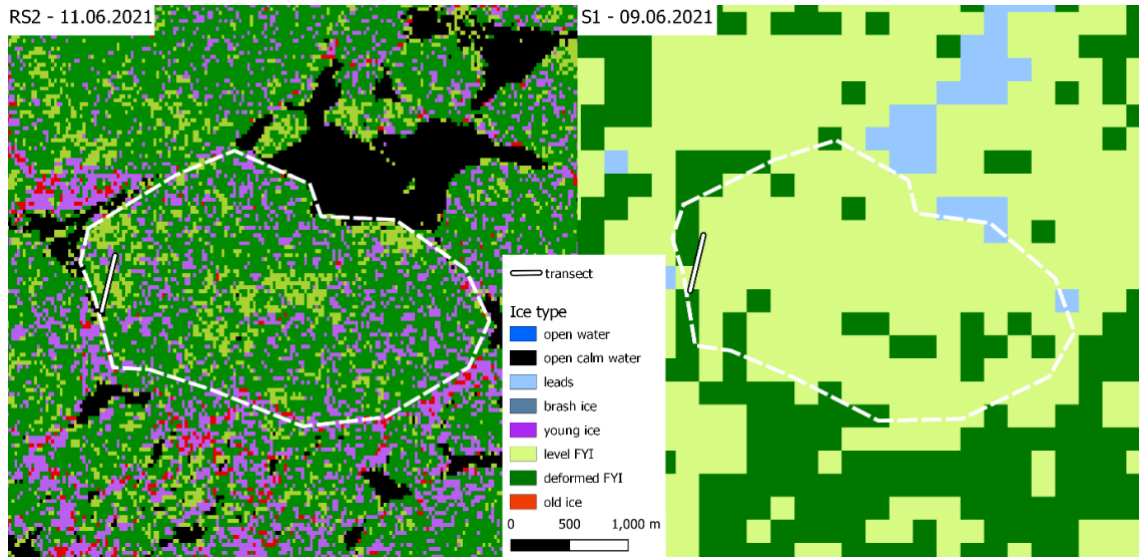


Figure 3.7. Ice station 1 classification results for the RADARSAT-2 (left) and Sentinel-1 (right) imagery. Data provided by NSC/KSAT under the Norwegian-Canadian Radarsat agreement 2021.

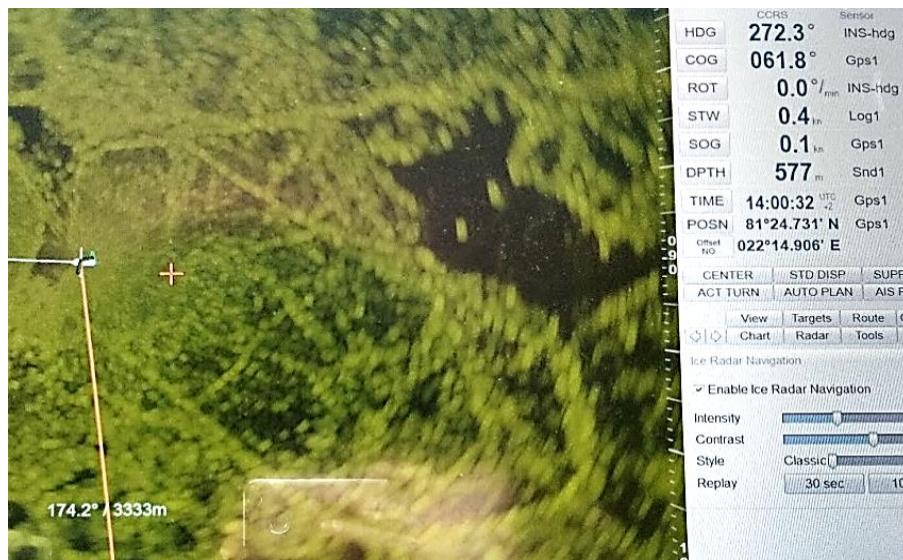


Figure 3.8. Image of the ship radar screen with the floe of the ice station 1.

Alongside the expected summer ice types (FYI & deformed FYI), atypical ice types such as young ice (purple) and old ice (red) were also classified (Fig. 3.7). The old ice misclassifications could be due to high brightness in the SAR backscatter image from large ridges within the deformed ice. The task of the fieldwork was to investigate the young ice misclassifications. The transect used for data collection are depicted as a white line in the Fig. 3.7 and red in the Fig 3.10.

Along the transect puddles of salty water were detected (Figs. 3.9 & 3.10), they were located near and in between ridges and were surrounded by relatively thinner ice. The salinity of these puddles indicates that they did not originate from thawing snow but were more likely from partly frozen leads or salty water coming out to the surface under the pressure due to ridging. A thick layer of salty slush was also observed over the FYI when ice cores were sampled (Figure 3.9).



Figure 3.9. 22 centimetres slush layer above the ice surface (on the left) and puddles of salty water (on the right). These puddles were also observed from the drone mosaic (Fig. 3.10) adjacent to the transect, alongside the sampling point (top right). These puddles and the thinner ice around them are likely what is classified as young ice in the sea ice type maps provided by classification algorithm.



Figure 3.10. Drone orthomosaic of the area above the transect at ice station 1 (red line) with the zoomed fragment of the mosaic at the top highlighting ponds of salty water and thin ice inclusions.

**Ice station 2**

Classification of a Sentinel-1 image was used since RADARSAT-2 data was unavailable. The imagery used had no additional multi-looking with a pixel size of 40x40m (Figure 3.11). According to the sea ice classification, the ice present is mostly level FYI with deformed FYI inclusions and old ice segments.

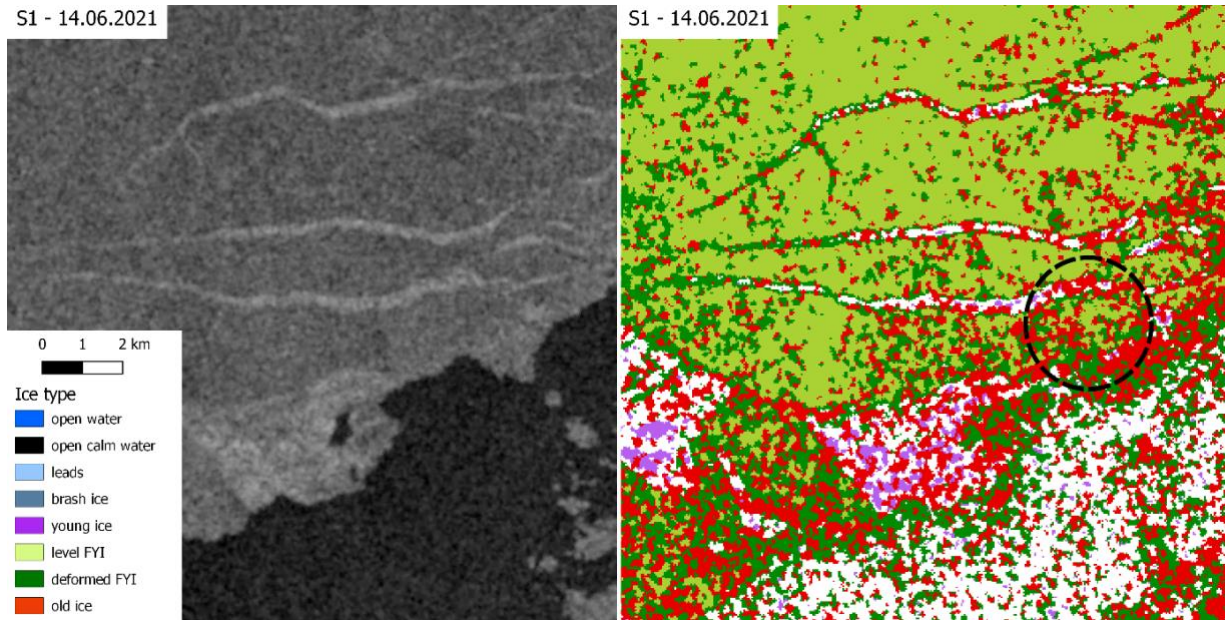


Figure 3.11. Sentinel-1 SAR image of the floe of station 2 (left) the classification result (right).

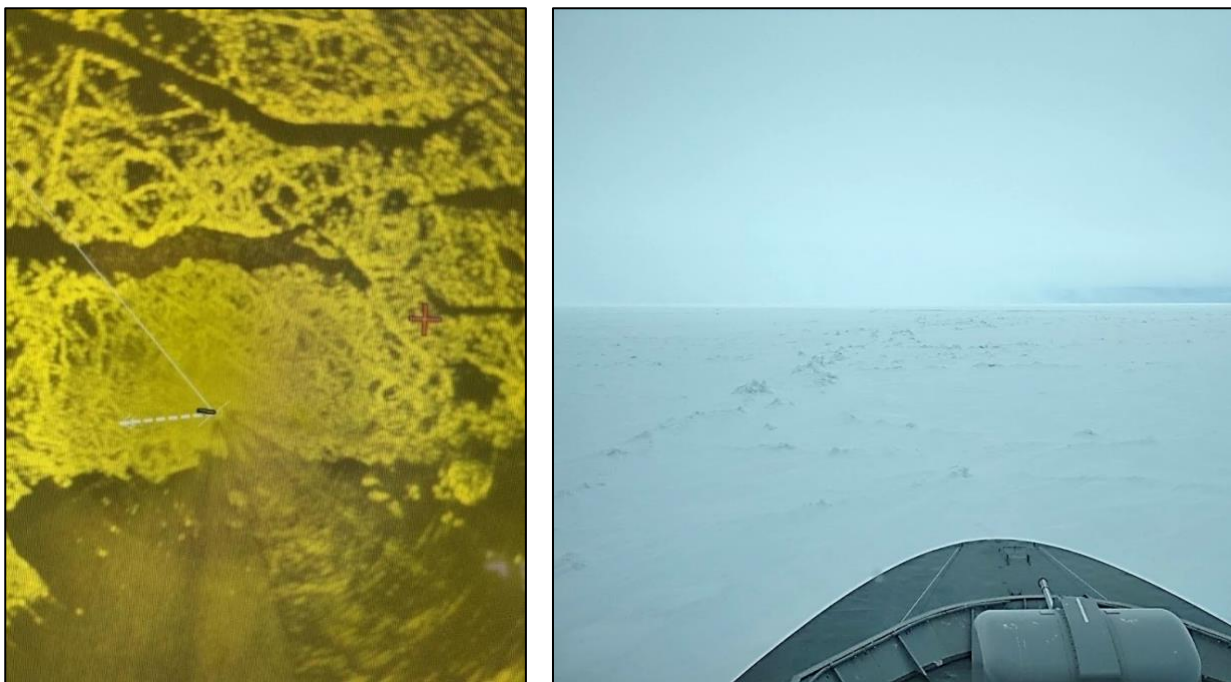


Figure 3.12. Image of the ship radar screen with the floe of the ice station 1 (on the left) and the photo taken from the bridge at the same time (on the right) where the sampling was undertaken.

Ship radar data and a photo taken from the (Fig. 3.12) show the area where transect 2 was undertaken. On the sea ice map (Fig. 3.11), this area is marked with the dashed black circle. The high density of red inclusions might be correlated with the higher concentration of the ridges in the left part of the circle that are also visible in Fig.3.12 from the bridge of the ship.

### 3.4 DISCUSSION

Based on the analysis of the classification results, two main questions arose. Firstly, how reliable is the deformed FYI type for the Sentinel-1 classification map and secondly what causes the young ice type inclusions within FYI during the melting season? Areas classified as deformed FYI (Fig. 3.6) are located closer to land and consequently are more exposed to compression processes causing deformation. However, the texture of big floes within this area do not seem to be more deformed than other floes to the North, potentially indicating that deformed FYI is overestimated. Additionally, it was observed that the SAR imagery around Svalbard was bright, this might relate to the incident angle and the 1<sup>st</sup> swath effect of Sentinel-1. However, classification results for images outside this area, and within a different swath, do not show big improvements in output.

Another possible explanation is that ice in this area was decaying and melting more intensively than to the North. In this case, water on the surface would cause a drop in the contrast and higher the brightness. This is supported by in situ data where a lot of slush was observed. For more precise conclusions, meteorological temperature data should be analysed to trace the same pattern in data distribution. Also, time-series data of ice formation and development in earlier months can help see what the history of deformation was and how strongly it effects the ice type distribution. Texture parameters can also be applied to see if it adds more reliable information for better classification results (Lohse et al., 2021).

For improving Sentinel-1 sea ice classification results for the ice station 1 and for more efficient comparison with the in situ data, processing results of higher spatial resolution could be also used. It was planned to use classification algorithm without 5x5 multi-looking. These results for the ice station 1 are presented in the Fig. 3.13 on the right. As the floe was within the 1<sup>st</sup> swath, ice types are classified wrongly, but relative distribution of the sea ice classes resembles the RADARSAT-2 image classification (Fig. 3.13), but further analysis is needed for different dates.

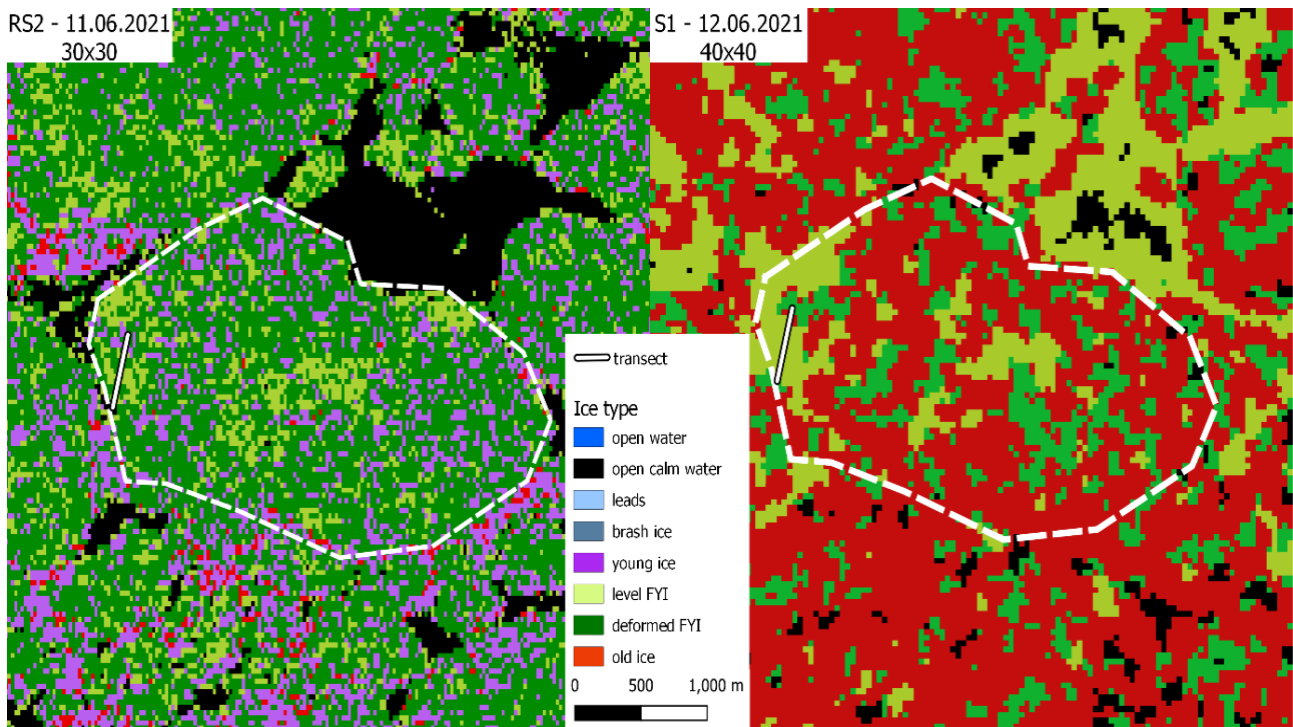


Figure 3.13. Comparison of the classification results for the RADARSAT-2 Quad-Pol (on the left) and the Sentinel1 EW (without multi-looking, on the right) images for the floe station 1. Data provided by NSC/KSAT under the Norwegian-Canadian Radarsat agreement 2021.

During the cruise, sensors onboard drones can also be deployed (weather dependent) to support the in situ sampling and bridge the gap between the sampling and coarser satellite data. At Ice station 1 a fixed wing Parot Disco with an RGB camera was able to successfully survey a large section of the ice floe along ~2km transects. These RGB images can be processed to create a high-resolution map that can then be used to visually identify ice features of the study sites. Structure from motion processing of the RGB drone imagery will also produce a 3D map of the ice surface providing further contextual information for satellite classification validation. Further work is required to understand the applicability and role of drone data for sea ice classification study.

### 3.5 REFERENCES

- Carrieres, T., Buehner, M., Lemieux, J.-F., Pedersen, L.T., 2017. *Sea Ice Analysis and Forecasting: Towards an Increased Reliance on Automated Prediction Systems*. Cambridge University Press.
- Dierking, W., 2013. Sea Ice Monitoring by Synthetic Aperture Radar. *Oceanography* 26, 100–111.
- Lohse, J., Doulgeris, A.P., Dierking, W., 2021. Incident Angle Dependence of Sentinel-1 Texture Features for Sea Ice Classification. *Remote Sensing* 13, 552. <https://doi.org/10.3390/rs13040552>
- Lohse, J., Doulgeris, A.P., Dierking, W., 2020. Mapping sea-ice types from Sentinel-1 considering the surface-type dependent effect of incidence angle. *Annals of Glaciology* 61, 260–270. <https://doi.org/10.1017/aog.2020.45>
- Sinha, N.K., Shokr, M., 2015. *Sea Ice: Physics and Remote Sensing*. John Wiley & Sons.
- Armstrong, T., 1972. World Meteorological Organization. WMO sea-ice nomenclature. Terminology, codes and illustrated glossary. Edition 1970. Geneva, Secretariat of the World Meteorological Organization, 1970.[ix], 147. (WMO/OMM/BMO, No. 259, TP. 145.). *Journal of Glaciology*, 11(61), pp.148-149.
- Zakhvatkina, N., Smirnov, V., Bychkova, I., 2019. Satellite SAR Data-based Sea Ice Classification: An Overview. *Geosciences* 9, 152. <https://doi.org/10.3390/geosciences9040152>

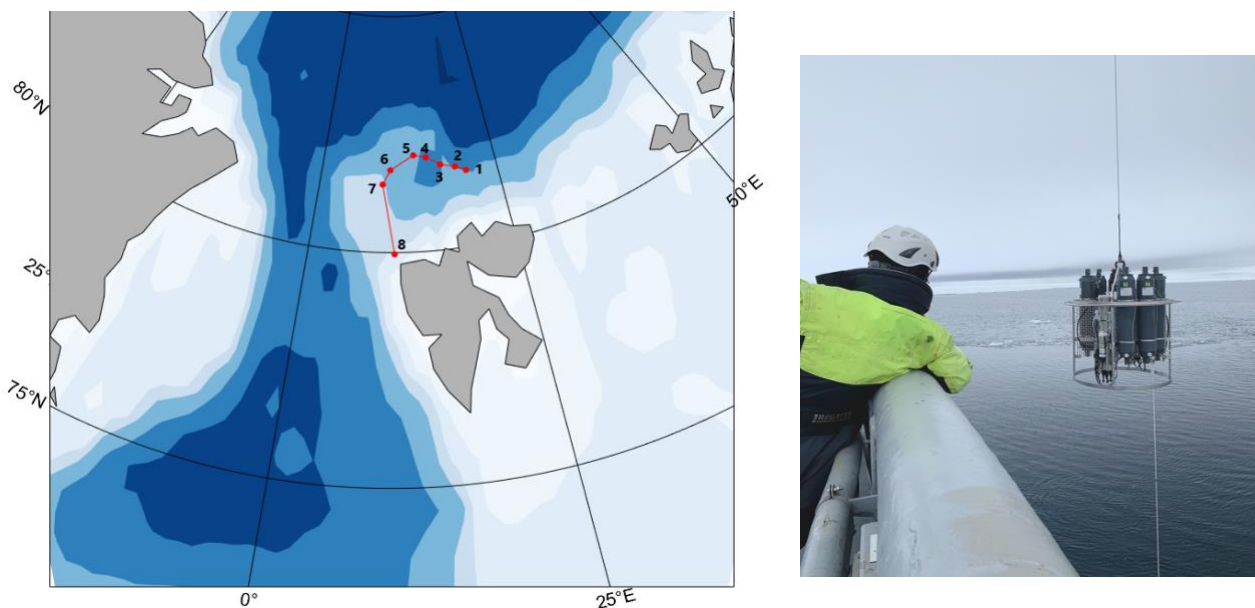
## 4. OCEAN OBSERVATIONS

Students: Astrid Stallemo, Anna Mathea Skar, Guney Dincturk, Mads Skjerven Moldrheim

Instructors: Agnieszka Beszczynska-Möller, Torill Hamre, Frode Monsen

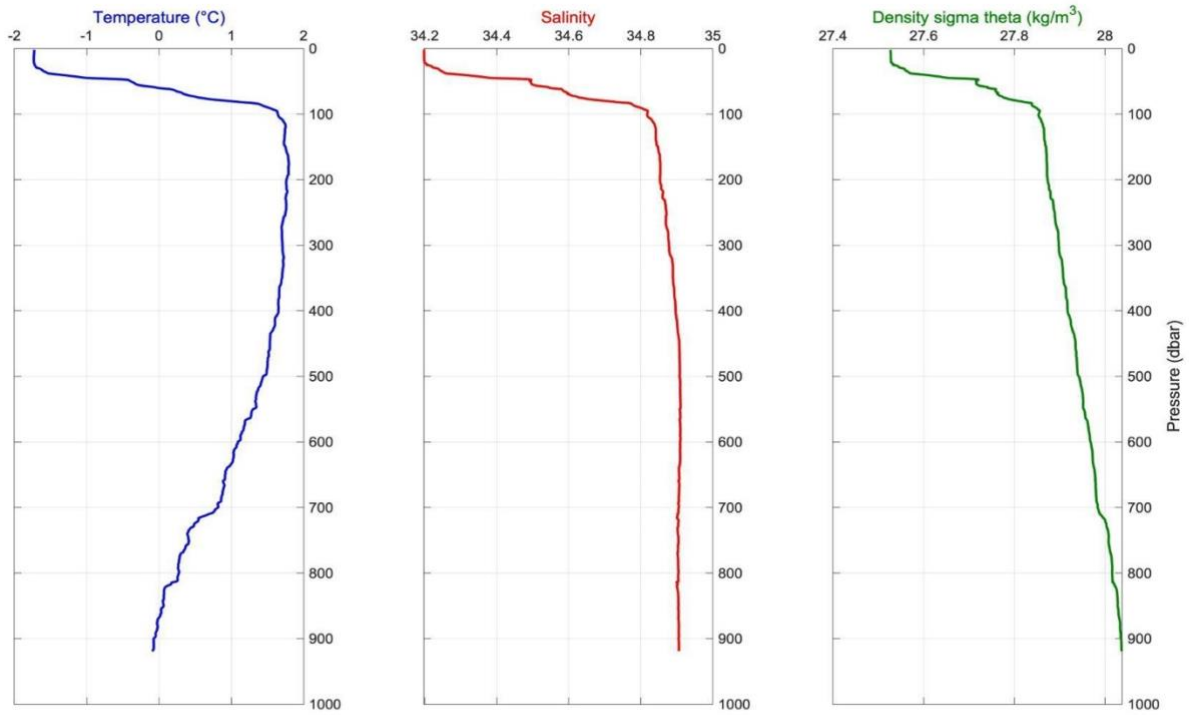
### 4.1 CTD DATA

During the UAK 2021 cruise we took 8 CTD stations north of Svalbard (Fig. 4.1). The transect was done between the 13<sup>th</sup> and 16<sup>th</sup> of June, starting at station 1. The depth range of station 1-7 was between 800 to 920 m. Whereas the depth of station 8 was at about 450 m, as we moved into a shallower part of the shelf closer to Svalbard. Figure 4.2 a and 4.2 b show vertical profiles of temperature, salinity, and density from station 1 and 8, respectively.



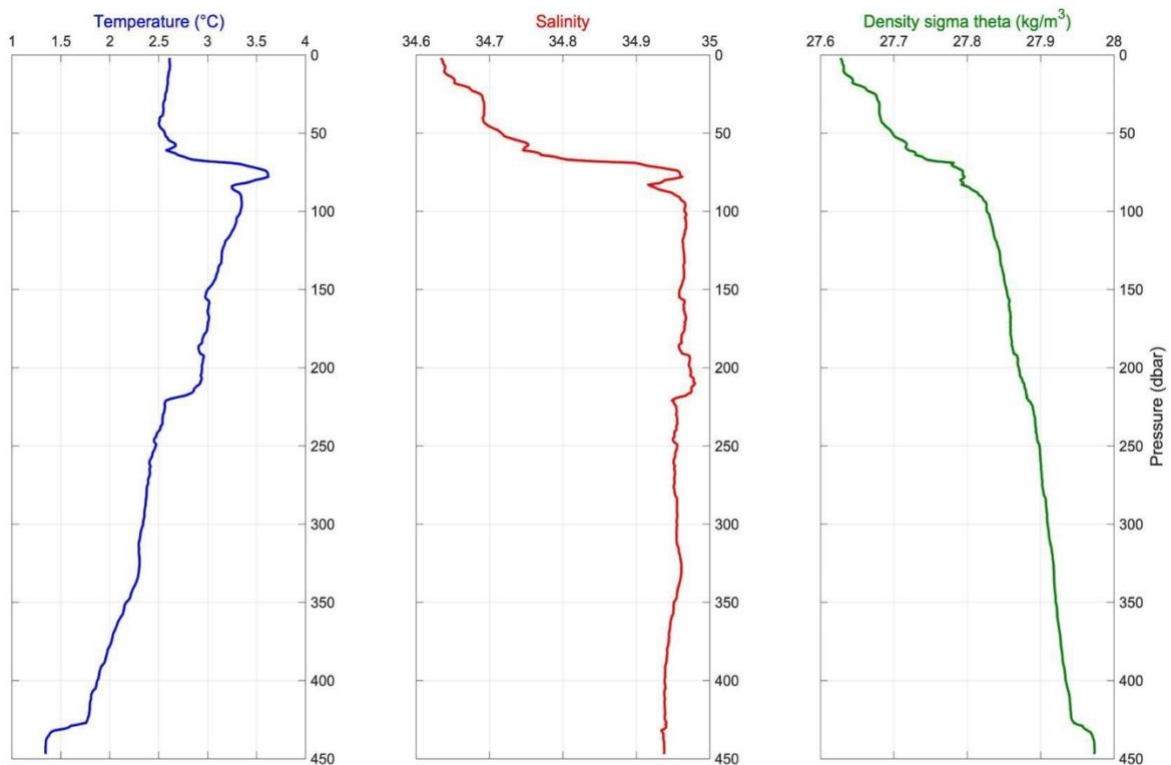
*Figure 4.1. Position of the CTD Stations obtained during the UAK 2021. The CTD rosette used from the AFT AOF KV Svalbard.*

Figure 4.2a and 4.2b show vertical profiles of temperature, salinity, and density from station 1 and 8, respectively. The temperature profiles from station 1 and 8 exhibit a clear difference and are therefore included in this report. The temperature measured at station 1 has near freezing-point temperatures ( $\sim -1.8$  °C) in the surface mixed layer (0 - 25 m). Atlantic origin water is found between 60 and 850 meters where the temperature is positive. At station 8 the Atlantic origin water is present throughout the whole water column (0 - 450 m). The temperature ranges between 1.4 °C and 3.6 °C, with the core (temperature maximum) at 75 meters depth.



Cruise: UAK2021 Station: UAK2021\_CTD\_001 Date: 13.06.2021 Time: 11:51 UTC Position: 81° 36.740'N 020° 34.470'E

Figure 4.2a. Vertical profiles of temperature (left), salinity (middle) and potential density (right) measured at station 1.



Cruise: UAK2021 Station: UAK2021\_CTD\_008 Date: 16.06.2021 Time: 12:08 UTC Position: 79° 57.800'N 010° 19.430'E

Figure 4.2b. Vertical profiles of temperature (left), salinity (middle) and potential density (right) measured at station 8.

## 4.2 INSTRUMENTS, PROCEDURE AND DATA PROCESSING

We used Seabird SBE 19plus V2 to measure conductivity, temperature and pressure (CTD). And we had six Niskin bottles mounted on the frame. Table 4.1 shows the accuracy, resolution and range of temperature and conductivity of the Seabird SBE 19plus V2. A GPS was connected directly into the box on deck, recording the location while measuring.

Table 4.1: Accuracy, resolution and range of temperature and conductivity for Seabird (SBE 19plus V2).

	Temperature accuracy (°C)	Temperature resolution (°C)	Temperature range (°C)	Conductivity accuracy	Conductivity resolution	Conductivity range
SBE 19plus V2	+/- 0.005	0.0001	-5 to +35	+/- 0.0005 (S/m)	0.00005 (S/m)	0 - 9 (S/m)

At each station, we lowered the CTD down to about 20 meters to flush the system. Then we brought it up to just below the surface, but we had to look out for drifting ice floes. We started recording and lowered the CTD down to target depth, which was set to 10 meters above the echo depth measured by the ship. Target depth of 10 meters above the echo depth was chosen to avoid lowering the CTD into the bottom, which can harm the instrumentation and frame. As an extra safety measure, a 10 meter line connected to an anchor was attached to a sensor on the frame. In case the anchor would hit sea bottom, the tension on the line would trigger a ‘bottom contact’ signal, and we could then stop lowering the CTD further down. In case of the ‘‘bottom contact’’ signal, we lifted the CTD until the signal disappeared, in case of uneven bathymetry. The CTD measures both on the up- and downcast. Data used in the files are from the downcast, as the data from the upcast is considered as a backup. We aimed to lower the CTD at a speed of 0.8 -1 m/s, and not over 1 m/s, in order to get a good resolution of the water column. Closer to the bottom we lowered the speed to avoid bottom contact.

The data files downloaded from the Seabird instrument comes in a specific format (type should be checked, probably described in the seabird software manual). We used the Seabird software to change the file format into cnv-files, as well as adding desired variables ( potential temperature, salinity, density, sound velocity) as these are calculated from the measured variables of conductivity, temperature and pressure. The data was averaged into 1 dbar bins and additional details on the processing can be found in the cnv-files. After getting the cnv-files, we converted the files into netCDF with the online data transformation tool, Rosetta available at <http://tomcat.nersc.no/rosetta/>.

## 4.3 BUOY, INSTRUMENTS, DEPLOYMENT AND RECOVERY

Contributors: Guney and Mads

The drifting ice buoy used during the UAK project 2021 is a custom buoy, designed by Woods Hole Oceanographic Institute. The buoy is floating within a hole drilled in the drifting ice sheet, which allows for measuring of the drift by instruments attached to the top. The buoy is connected to a 34m long cable that goes into the ocean. At the end of that wire, there is a cage holding a CTD and a CAT pinger, and a weight below the cage. In addition, there is a hydrophone clamped onto the wire. While the ice is drifting, acoustic sounds in the ocean and CTD measurements are collected by instruments. All the instruments relating to the buoy will be described in greater detail below.

### 4.3.1 SBE37 MicroCAT

The SBE37 MicroCAT made by Sea-Bird Scientific is a CTD-instrument. Placed in the cage at the end of the cable at an approximate depth of 34 meters, the instrument collected data on pressure, temperature and salinity

for the duration of the deployment. The data is presented in the four graphs below, where pressure, temperature and salinity are presented in separate graphs at first and then finally united in a single graph.



Figure 4.3: To the right the flotation device with the Iridium beacon, GPS device and radio beacon. In the middle the 34 m wire The cage and the weight with the CAT pinger, the hydrophone, MicroCAT, Iridium beacon, LED Flasher and radio beacon

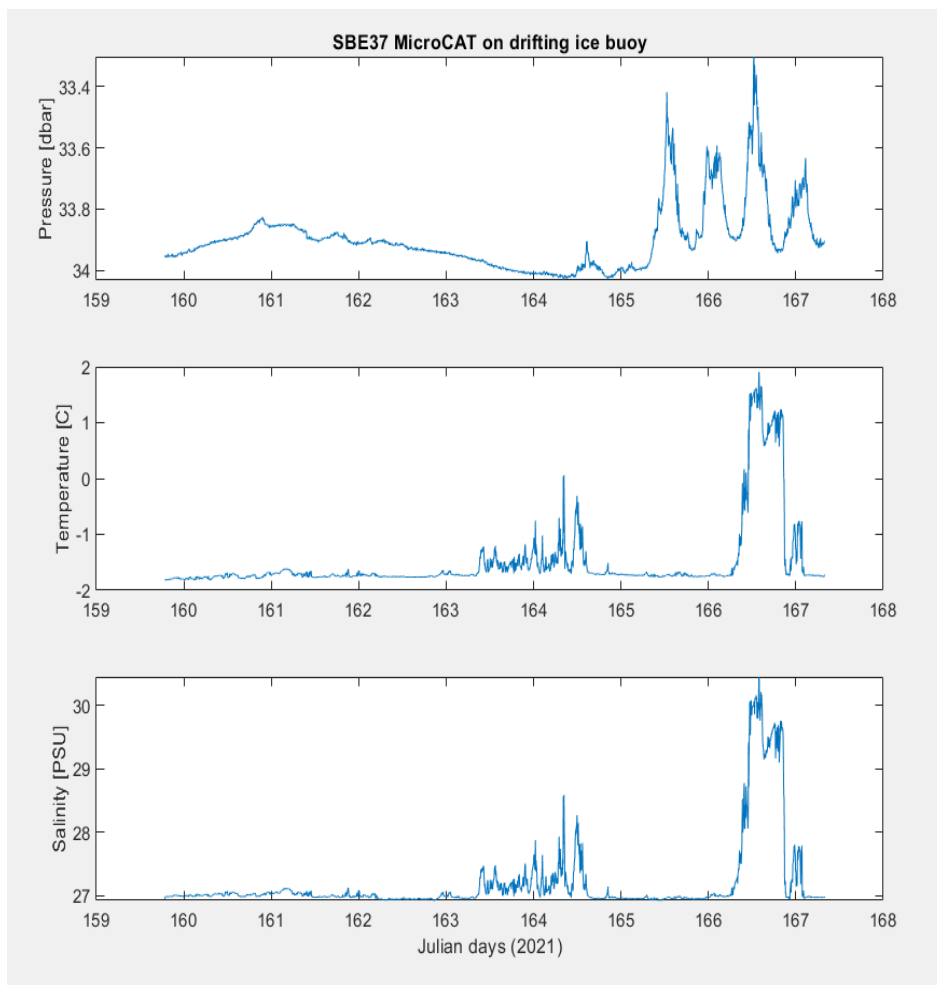


Figure 4.4: CTD-data collected by the SBE37 MicroCAT on the drifting buoy presented in three separate graphs

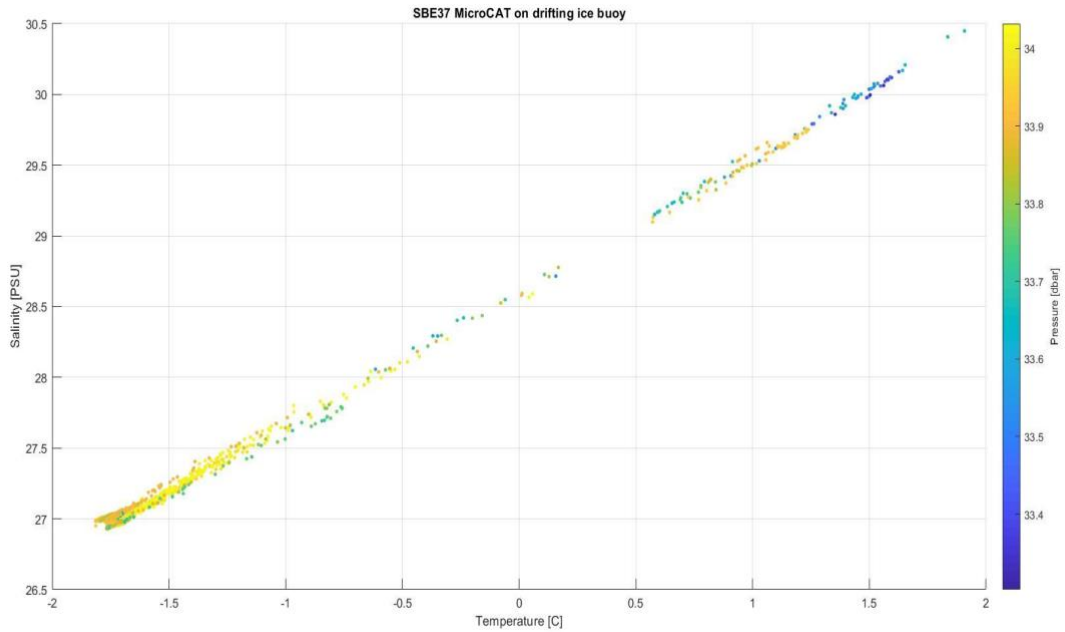


Figure 4.5: CTD-data collected by the SBE37 MicroCAT on the drifting buoy presented in together in a single graph

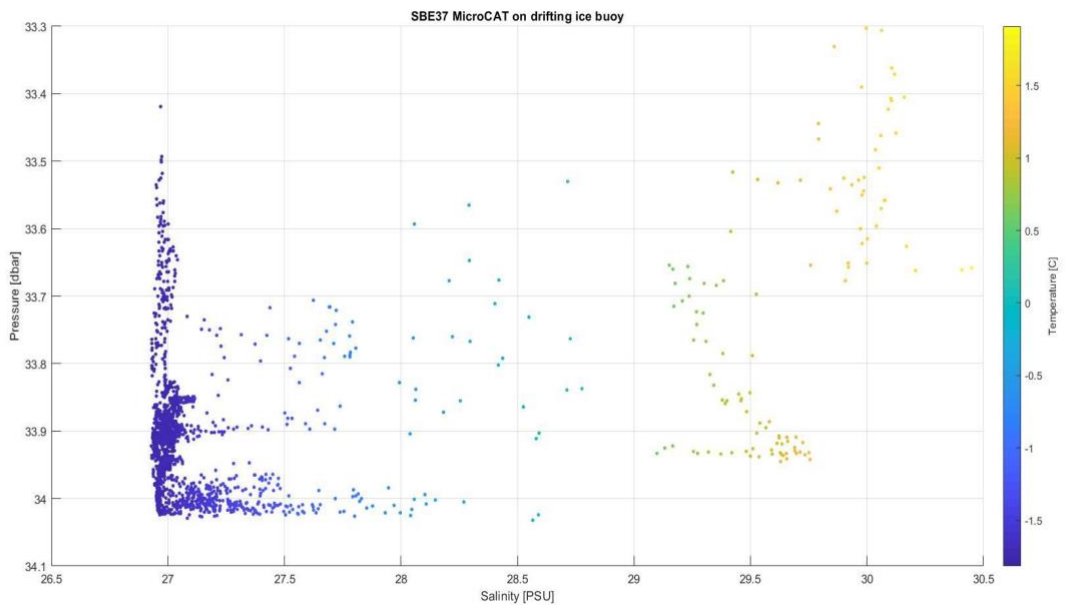


Figure 4.6: CTD-data collected by the SBE37 MicroCAT on the drifting buoy presented in three separate graphs

### 4.3.2 Kilo Iridium Beacon

The Kilo Iridium Beacon made by Xeos Technologies is a device used for tracking the position of the buoy. It was fastened to the top of the buoy and used for logging and transmitting GPS data. The transmission happens through iridium satellites. A map containing the logged GPS-data is shown in Fig.4.7.

UAK 2021 - Drifting buoy

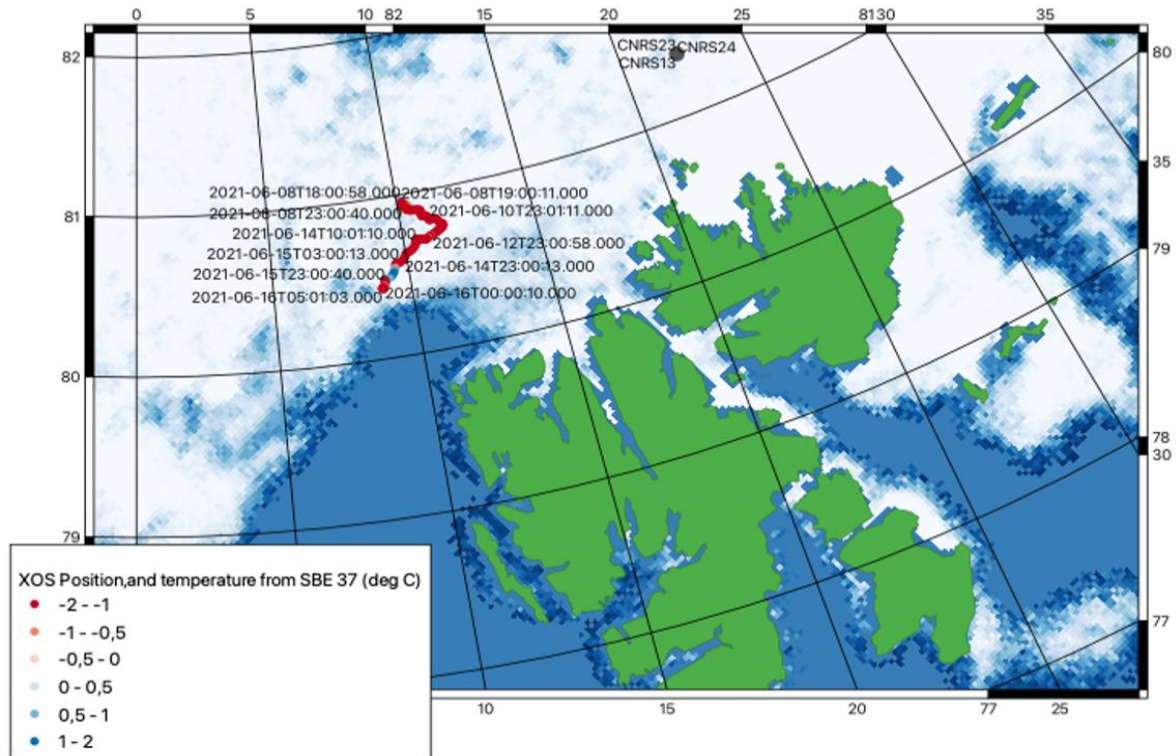


Figure 4.7: Position of the buoy as logged by the Kilo Iridium Beacon.

### 4.3.3 EdgeTech CAT Pinger

The Coastal Acoustic Transponder (CAT) made by EdgeTech is an instrument designed for underwater location. Placed in the cage at the end of the cable at an approximate depth of 34 meters, it was used in an exercise in acoustic triangulation which is explained in greater detail in the section concerning acoustics.

### 4.3.4 MTE $\mu$ AURAL

The micro Autonomous Underwater Recorder for Acoustic Listening ( $\mu$ AURAL) is a hydrophone. Attached to the cable of the buoy, it recorded sound at a high sampling rate. Relevant sounds are ship traffic, marine mammals, ice cracks, bubbles and splashing water. See section 5.

### 4.3.5 XMB-11K Radio Beacon

Made by Xeos Technologies, this device was mounted to the top of the buoy. It transmits radio signals which are used for locating the buoy. It was used together with the Iridium Beacon, where the Iridium Beacon was used for a larger scale and the Radio Beacon was used on a small scale.

### 4.3.6 XMF-11k LED Flasher

Also made by Xeos Technologies, this device is a super-bright LED that flashes at certain intervals. Mounted to the top of the buoy, it can be used for positioning in challenging conditions. As we had good weather and midnight sun, it was not relevant for our recovery of the buoy. However, in the case that we were prevented from recovering the buoy during the cruise, it could have been useful if a recovery were to happen during winter.

### 4.3.7 Buoy Deployment

The buoy was deployed on the 8th of June. All of the parts for the buoy were brought out onto the ice for assembly. The CTD scanner and the CAT pinger were inserted into the cage and the hydrophone was clamped onto the middle of the wire. A hole was made for the buoy to lay inside. The hydrophone was turned on with a magnet and it was ready to be deployed. Part by part the cage and the wire was carefully lowered into the hole to not damage any instruments. It was checked that the iridium beacon was visible from the ship's radar and it was ready to be left there.

### 4.3.8 Buoy Recovery

When the data acquisition had been done, the buoy recovery operation started. The buoy position was located with both the iridium beacon and radio beacon. The KV Svalbard was parked by the ice sheet where the buoy was deployed 8 days before. Scientific crew and polar bear guards went out of the ship and recovered the buoy with instruments attached to the wire. The ice had become much thinner and more fragile since the last time so we had to be careful where to walk and wear floatation suits. The buoy was lifted carefully out of the hole and each instrument was detached and brought onto KV Svalbard.

## 4.4 DRIFTERS

In total, 3 drifters were deployed on the sea ice in the Svalbard area for the International Arctic Buoy Program (IABP). These types of drifters are distributed by Data Buoy Instrumentation (LLC) and tracked and logged by the U.S. Department of Commerce NOAA (National Oceanographic and Atmospheric Administration). These types of drifters are deployed globally, tracking pressure, temperature and GPS positions.

The drifters consist of a surface float that keeps the drifter afloat and a drogue that keeps them stable in the water and makes them move more consistently with the currents. The surface float has sensors attached that measures sea level pressure (SLP) and temperature. The antenna on top transmits the data and GPS location. They are activated by removing a magnet from the buoy that will trigger the drifter to start tracking. It will do so for the amount of time they have been programmed to or until they get lost. A model of the drifter is shown in Fig 4.8.



Figure 4.8: Model of the drifting buoys. A drifter successfully placed on a large ice floe. The drogue will open when the drifter goes in the water.

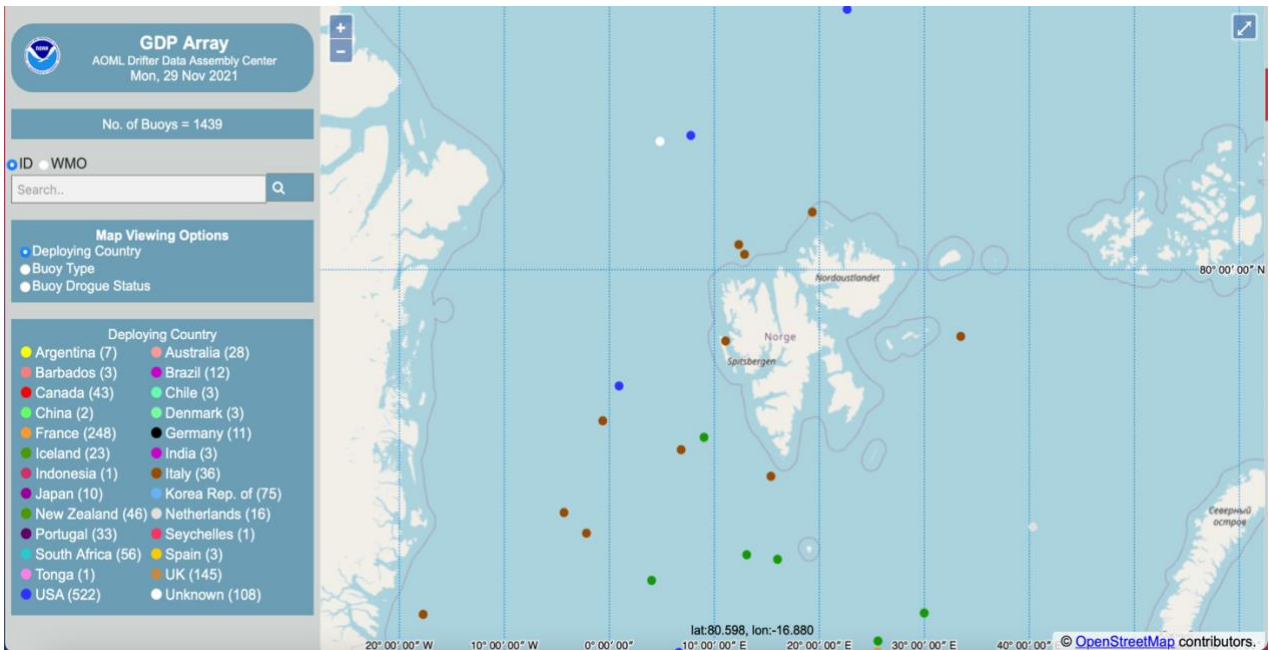


Figure 4.9: A snapshot of the distribution of the drifters in the Global Drifter Program in the Svalbard area.

The drifter IDs that we placed on the sea ice and activated were 61182960, 61084040 and 61759270. They all had an expected lifetime of over one year. As per 01.12.21, none of the drifters are searchable or visible on the map, meaning they are most likely lost under the ice. Below is the Drifter ID Card of drifter 61084040 per 01.11.21 (Fig. 4.9). This drifter was deployed at position 81°4'30N 22°4'90E. As we can see from the raw data in Fig. 4.10, the drifter was likely on the ice floe until the start of August when it went into the water as the temperatures are more stable after this point.

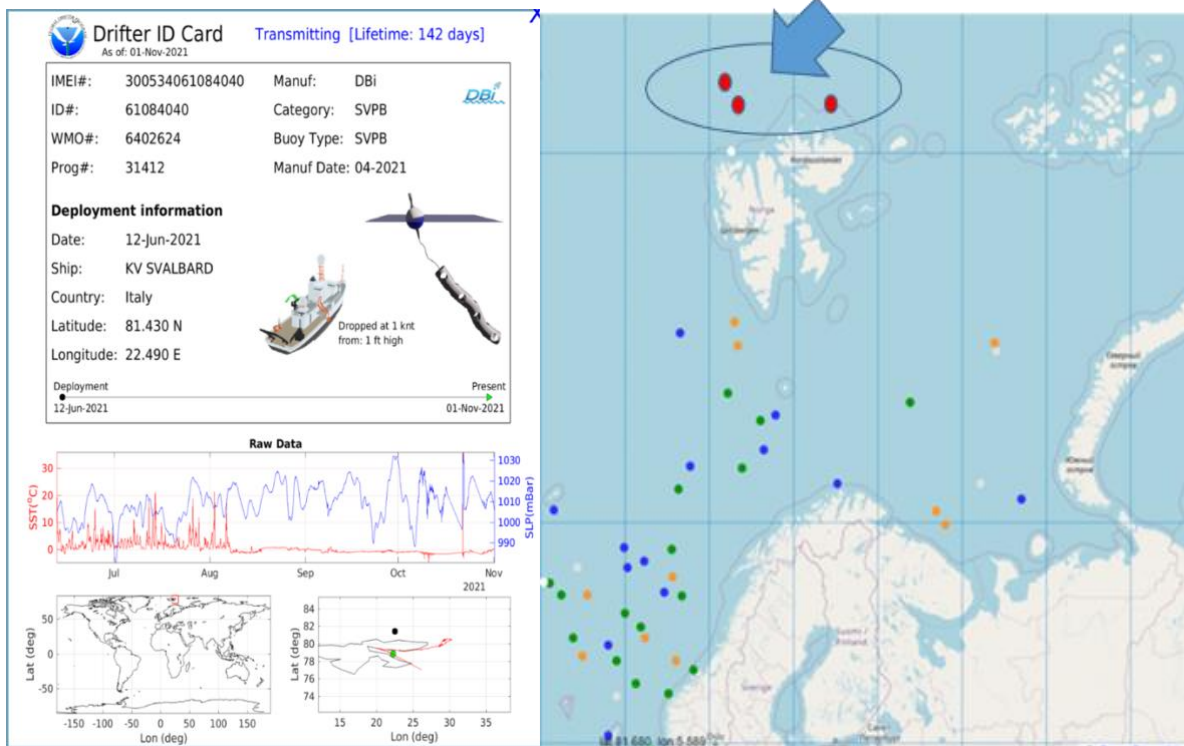


Figure 4.10: Left: Drifter ID card and raw data. Right: Initial location of the 3 drifters north of Svalbard.

## 5. ACOUSTIC MEASUREMENTS

Authors: William Jenkins, Hayden Johnson, Meghan Helmberger, Sofia Vakhutinsky

Instructors: Espen Storheim, Hanne Sagen

The acoustic work reported below is published in Jenkins et al. 2022.

### 5.1 INTRODUCTION

During the UAK 2021 cruise, a series of measurements and observations were made over the course of eight days utilizing both passive and active acoustics. On 8 June, a drifter buoy with several instruments was deployed in an ice floe and left to passively record for eight days. An acoustic localization of the buoy was demonstrated before KV Svalbard continued on with her cruise. At various points in the subsequent week, KV Svalbard fastened herself to ice floes where measurements of the ice were made. At each of these ice stations, passive acoustic observations were made. On 12 June, acoustic localization was used to successfully estimate the position of an oceanographic mooring for recovery. On 16 June, KV Svalbard located and recovered the drifter buoy, whose data are presented for analysis.

The purpose of the acoustic tasks was to introduce the students to practical applications of underwater acoustics, including equipment selection and preparation, mooring construction, deck handling, and data collection and handling. Furthermore, students observed the ocean environment and its role in underwater acoustic propagation. Finally, students learned the utility and value of using underwater acoustics for operations in the Arctic Ocean, particularly in location and retrieval of equipment and in measuring the environment.

### 5.2 DRIFTER BUOY

#### 5.2.1 Equipment, Deployment, and Recovery

The drifter buoy consisted of a weighted line approximately 35 m long suspended from a float (Fig. 5.1). A Multi-électronique uAURAL recorder with an integrated HTI 96-min hydrophone, sampling continuously at 48 kHz sampling frequency, was mounted on the line at 30 m depth. A Sea-Bird Scientific SBE37 CTD, sampling with an interval of 5 minutes, was mounted at 33 m depth. A XEOS GPS receiver was fastened to the float itself, and recorded the position of the float every hour. An Edgetech Coastal Acoustic Transponder (CAT) was mounted for acoustic localization.



The buoy was deployed on 8 June 2021 at approximately 17:52 CET, at 80° 57.855' N and 010° 09.437' E. To ensure the buoy remained fixed to the ice floe, a hole was drilled through the ice large enough for the instruments to pass through, but small enough that the float would remain lodged at the surface. In the event the ice floe were to melt or fail, the float ensured the instruments would not sink.

Figure 5.1 Photo of the float on top of the ice.

The drifting buoy and hydrophone were picked up on 16 June at 09:09 CET at 80.43409 and 8.98896. The buoy's GPS transceiver provided general localization, and as KV Svalbard approached, the buoy was identified visually. The buoy had cumulatively traveled 108.7 km, and as seen in Figure 5.2, initially drifted southeast, then changed directions to the southwest.

## 5.2.2 Data Analysis

The ice floe that the drifter was fastened to was observed to have thinned over the course of the deployment, with a measured ice thickness of about 70 cm at the start of the deployment and about 30 cm upon recovery. Previous studies (e.g. Mahanty et al. 2020) have suggested that melting sea ice produces sound in the underwater environment, in the frequency range of a few hundred Hz to a few kHz. To assess whether this signal is observable in our data, we compare the sound power measured by the hydrophone in several frequency bands to measured or modeled (taken from the ECMWF ERA5 reanalysis product) environmental variables which could reasonably be expected to be indicative of melting of the sea ice near the drifter.

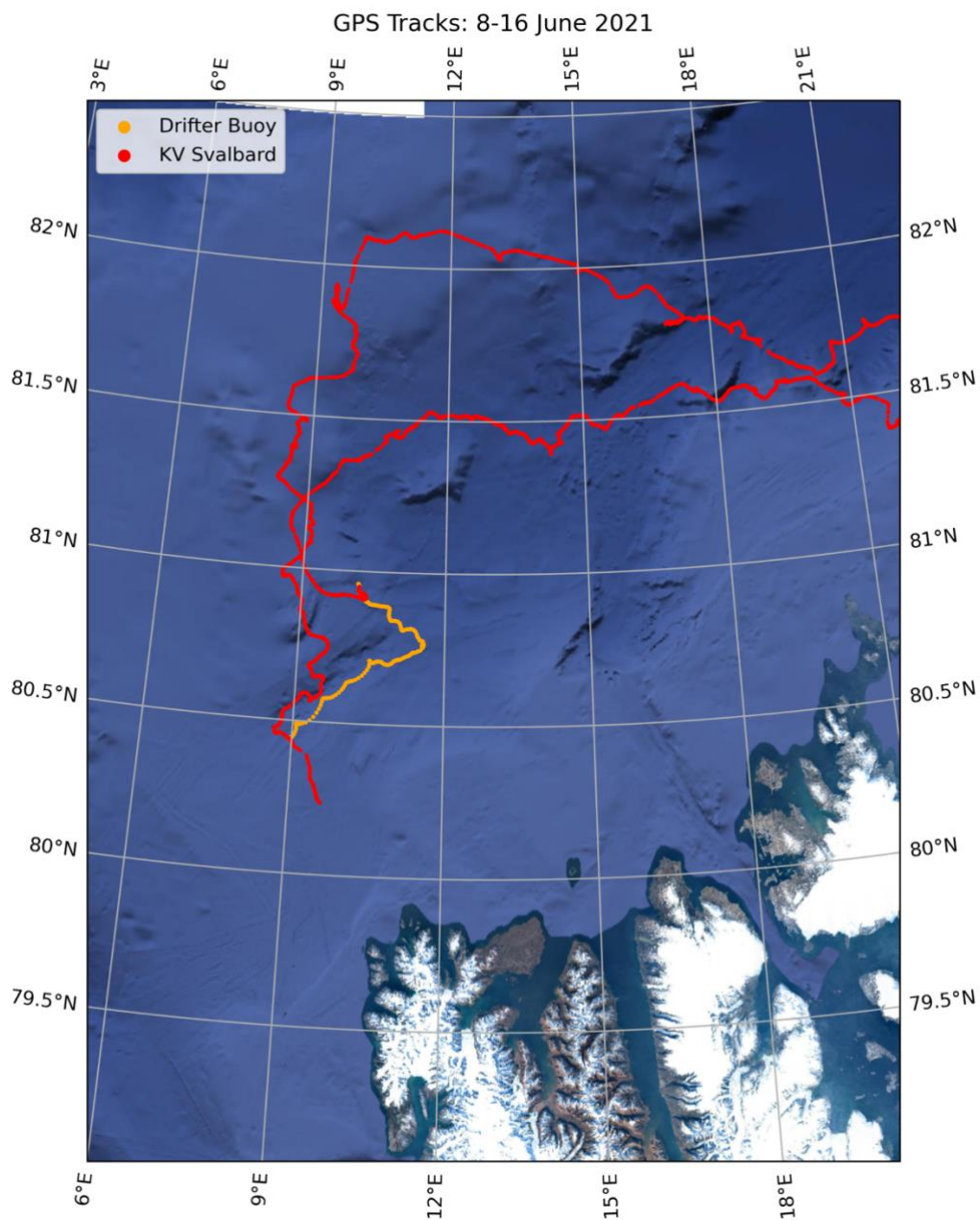


Figure 5.2. Map showing the track of the KV Svalbard (red) and the drifting buoy (orange) over the period of the drifter deployment.

Table 5.1. Correlation between various environmental factors and the logarithm of sound power integrated over different frequency bands.

	0-0.3 kHz	0.3-1 kHz	1-3 kHz	3-10 kHz	10-24 kHz
Water temperature	0.1004	0.0662	0.0943	0.1351	-0.0093
Buoy speed over ground	0.4707	-0.0241	0.0603	0.0828	-0.0950
ERA5 10m wind speed	0.6358	0.1232	0.2302	0.3216	0.0169
ERA5 2m air temperature	0.2349	-0.0900	-0.0452	-0.0272	-0.1085

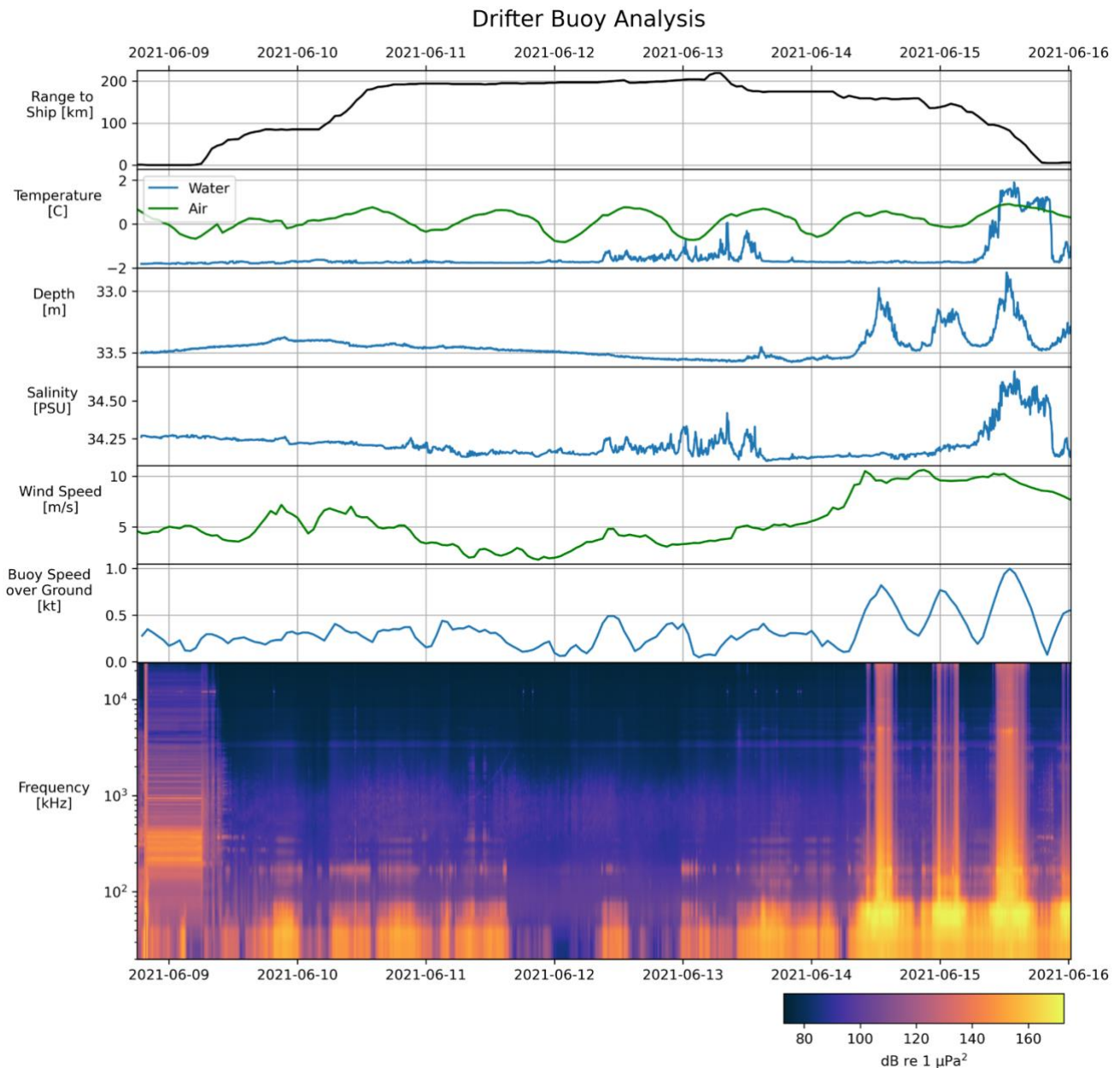


Figure 5.3. Time series of various environmental variables, which were measured by the drifter CTD (water temperature, salinity), the drifter GPS (buoy speed over ground, range to ship), or taken from ERA5 reanalysis products (air temperature, wind speed). The bottom panel is a spectrogram of the acoustic data recorded by the hydrophone over the duration of the deployment, showing the distribution of energy over frequencies. Note that the sharp vertically uniform bands of high energy are periods where the sound was sufficiently loud to saturate the recording; these periods have accordingly been removed from the analysis presented in table 5.1.

It is apparent visually from Figure 5.3, and from the correlations presented in Table 3.1, that the dominant feature in the integrated sound power is an increase in the energy present at low frequencies corresponding to times when the over-ground speed of the drifter and the ERA5 10 m wind speed. By listening to the recordings, it was determined that most of this energy is likely a result of strum noise due to the motion of the drifter through the water. The depth of the CTD, computed from the measured pressure, can be seen to decrease at the periods with the highest speed over ground, suggesting that there was sufficient force being exerted on the cable and instrumentation to cause the line to tilt away from vertical, which adds support for the hypothesis of strum noise. It seems likely that the correlation between wind speed and sound power at low frequencies is at least partially a result of the causal relationship between wind speed and the speed of the ice flows, which determines the speed of the drifter. However, the weak but still elevated correlations between wind speed and sound power even at high frequencies, where buoy speed over ground and sound power are completely uncorrelated, suggests that wind acting on the available area of open water could be causing some increase in underwater noise.

Even outside the low-frequency band dominated by the strum noise, we find no clear relationship between the environmental variables that might be indicative of melting and the sound power in any frequency band. The slight rise in water temperature during the middle of the record does not correspond to any discernible increase in sound power, and the rise in water temperature near the end of the record unfortunately corresponds with a period of hydrophone saturation.

### 5.2.3 Drifter Buoy: Highlights

In this section, we highlight some signals recorded by the drifter buoy that were representative of the broader soundscape observed during the recording period. The biologic examples that follow were excerpted from the morning of 12 June when the record had the lowest ambient and self noise. During this quiet period, many types of marine mammals and fish vocalizations could be heard. Identification of the species based on the vocalization characteristics was attempted using the Discovery of Sound in the Sea (DOSITS) website; however, the audio examples on the website are somewhat limited, and it was not possible to positively identify all of the vocalizations. Of interest, whale vocalizations consisting of songs and pulses were heard, although species identification was not possible using the DOSITS website.

Though the data from the morning of 12 June can be readily analyzed for biologic sources, it is noteworthy that, in spite of the noise of the strumming buoy wire, biologic sources were detected throughout the entirety of the record. The most prominent and easily identifiable sources were bearded seals. Cetaceans were also heard throughout the record and were most likely narwhals or dolphins. Throughout the record, broadband pops and clicks were observed, some of which were likely associated with echolocation from marine mammals, although species attribution based on a single impulse was not possible..

In addition to biologic sources of sound, several anthropogenic sounds were observed throughout the record. Machinery, propulsion, and icebreaking from KV *Svalbard* is heard in the first two days of the record, and a periodic 150 Hz tone was recorded every five minutes throughout the entire record.

#### ***KV Svalbard: Rotating machinery***

After deploying the drifter buoy, KV *Svalbard* continued to drift with the ice floe overnight with her drives secured. Of course, various hotel loads and machinery continued operating. In recordings made near KV *Svalbard*, including those from later ice stations, a periodic clicking noise was heard and is shown in the spectrogram in Figure 5.4, with a stronger click followed by a weaker click. The period of the full cycle was 1.75 s. Owing to the regular periodicity of this signal, it is likely generated by a rotating piece of machinery operating at approximately 34.3 RPM.

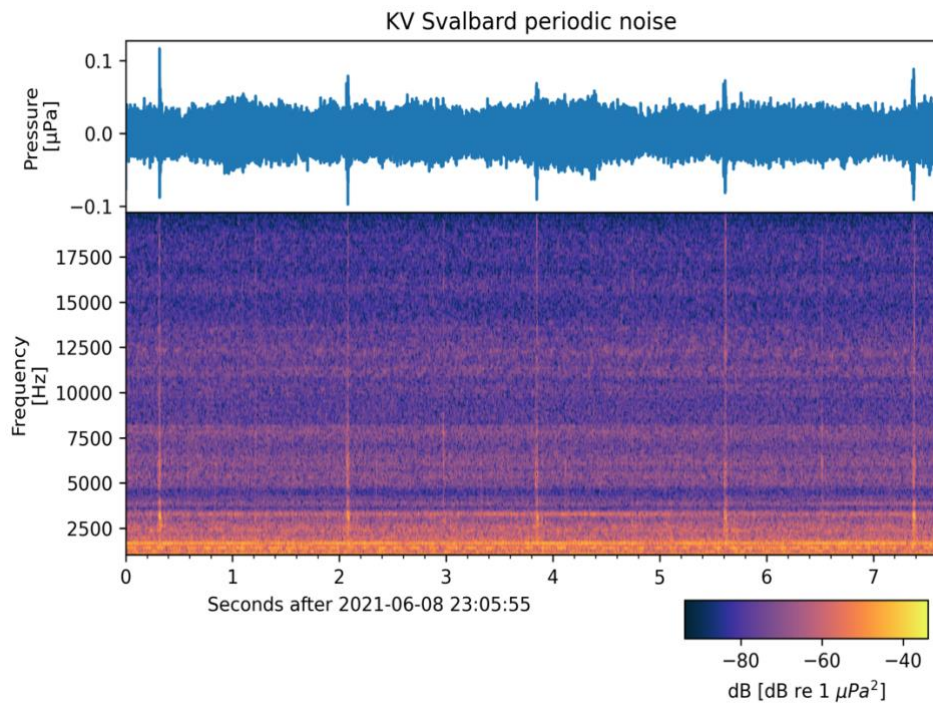


Figure 5.4. Periodic transients from KV Svalbard suggest rotating machinery as the source.

**KV Svalbard: Maneuvering through sea ice**

KV Svalbard was underway again on the morning of 9 June to conduct acoustic ranging to the drifter buoy. Figure 5.5 shows a spectrogram of KV Svalbard maneuvering through sea ice. Below 1.5 kHz the propulsion machinery dominates the spectrum. Above 1.5 kHz, the spectrum becomes saturated with broadband noise as the ship impinges on ice and breaks it apart. Areas of open water are indicated by regions of low energy above 1.5 kHz.

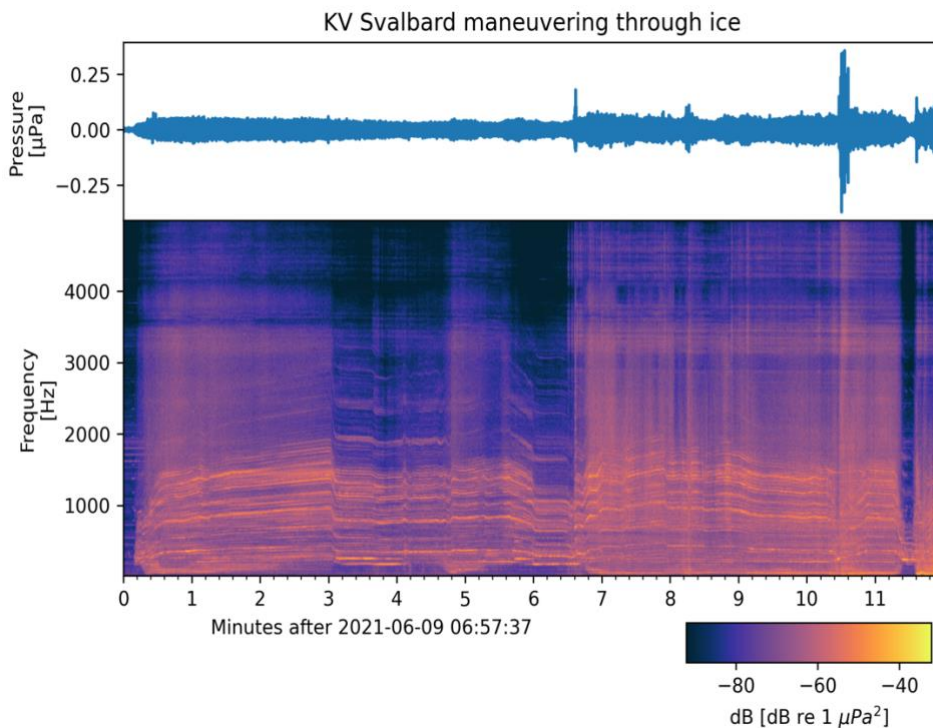


Figure 5.5. KV Svalbard maneuvering through sea ice.

### Coastal Acoustic Transducer (CAT) Pinger

The Edgetech CAT pinger worked in tandem with a shipboard transducer to perform active acoustic localization. On board KV *Svalbard*, a deck unit drove a transducer that produced an 11 kHz outbound signal. The CAT, upon receiving the 11 kHz signal, transmitted a 12 kHz signal. On board *Svalbard*, the time elapsed between the transmission of the 11 kHz signal and receipt of the 12 kHz signal constituted the two-way travel time. Assuming an average speed of sound in water, the distance between the source and receiver could be estimated (see section 3.3 for detail). In Figure 5.6, a spectrogram of the sequence of localization signals is shown. An 11 kHz tone is broadcast by the ship, followed immediately by the 12 kHz response from the CAT attached to the buoy.

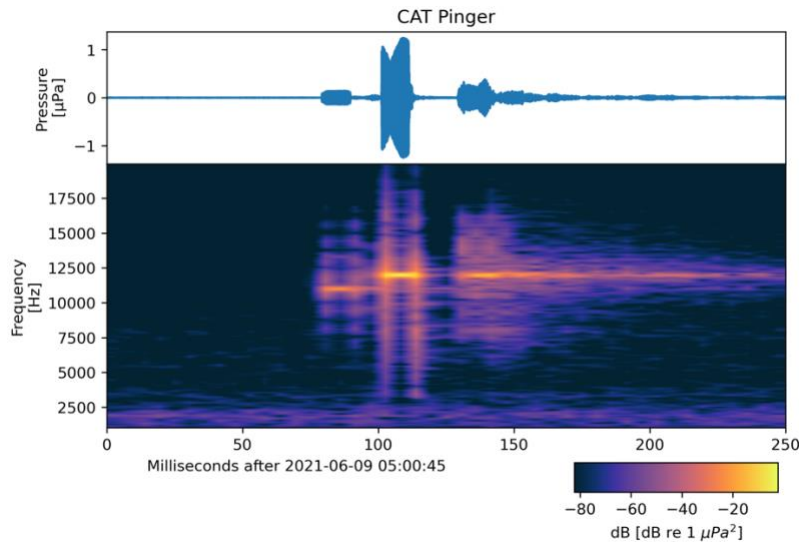


Figure 5.6. Acoustic localization signals. The 11 kHz tone was transmitted by KV *Svalbard*, and the 12 kHz tone was the response transmitted by the transducer on the drifter buoy.

### Bearded Seals

Bearded seals were heard constantly throughout the entire record. These seals emit a warbling sound that sweeps downward in frequency, with occasional upshifts. From Figure 5.7, the duration of some of these calls was greater than one minute. As June was in the middle of their mating season, these calls may be attempts to attract mates. Bearded seals were spotted from KV *Svalbard* on sea ice throughout the cruise.

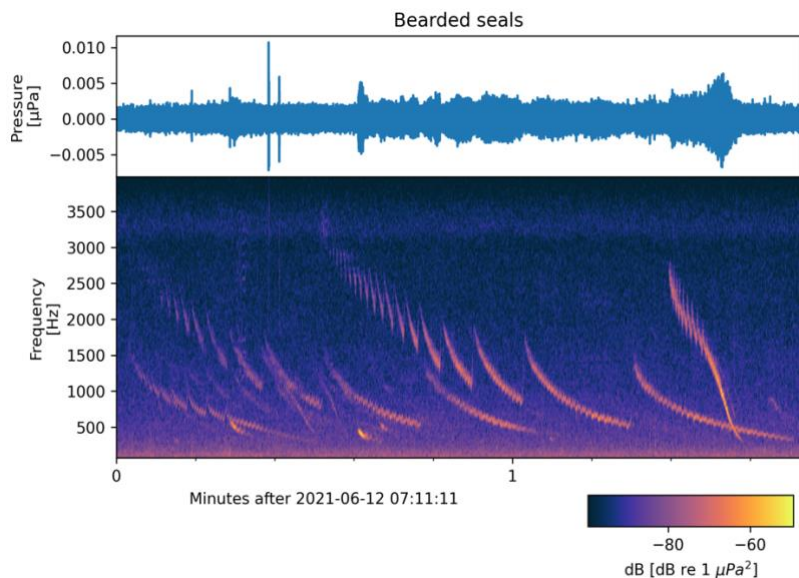


Figure 5.7. Bearded seal vocalizations.

### Marine Mammals

Figure 5.8 shows examples of vocalizations from several biologic sources. The long, warbling downsweep of a bearded seal is visible below 1 kHz over the course of the entire spectrogram. Fine striations above 1 kHz sweeping rapidly up and down are likely narwhals or dolphins and were heard throughout the entire record. An unknown vocalization with fundamental frequency at approximately 1.3 kHz and harmonics at 700 Hz intervals is observed with a single call at 2 seconds, followed by a repetitive train of pulses between 8 and 12 seconds. Vocalizations occurring at 7.5 seconds between 200 Hz and 300 Hz may either be whale vocalizations or bearded seals.

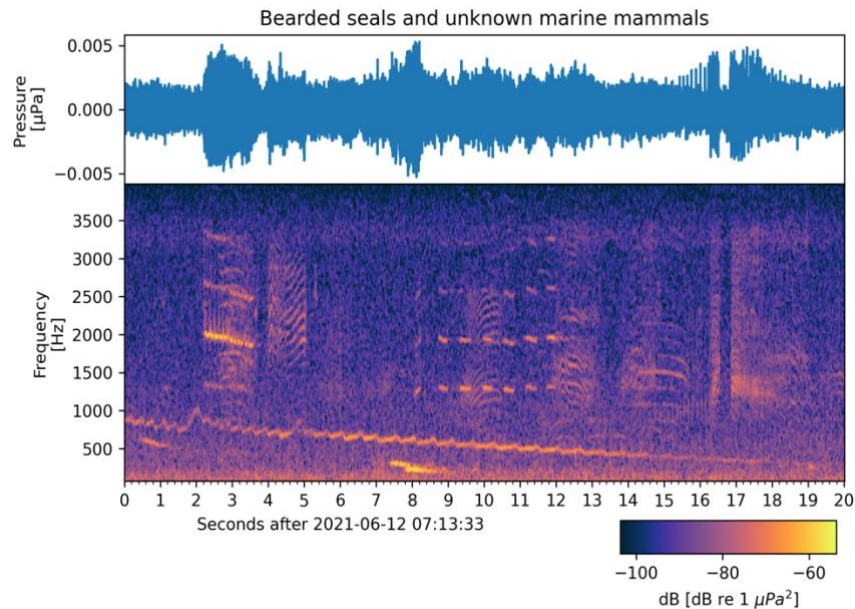


Figure 5.8 Marine mammal vocalizations, including a downsweep made by a bearded seal (below 1 kHz) and cetacean vocalizations.

### Low-frequency Tone

Throughout the entire deployment, a 150 Hz tone with 1 s duration was recorded precisely every five minutes. The persistence and regularity of the tone suggests the source is anthropogenic and may be a tomographic source. A representative example taken from 11 June is shown in Figure 5.9.

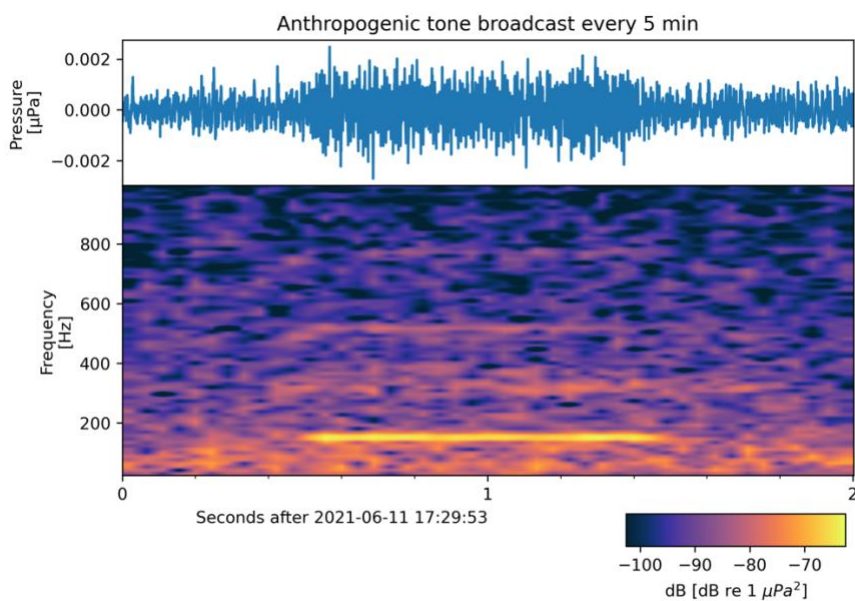


Figure 5.9. Anthropogenic 150 Hz tone that was recorded precisely every five minutes over the course of the buoy deployment.

**Unknown Animal**

One of the biologic sources was recorded on numerous occasions between 10-13 June. This animal would emit single vocalizations as well as call repeatedly two to three times per minute for several minutes. The vocalization sounds like a deep, nasal “wow,” with the beginning of the signal shifting downward in frequency, and at the very end sweeping up. Figure 5.10 shows the vocalization in detail, and Figure 5.11 shows its co-occurrence with a bearded seal vocalization.

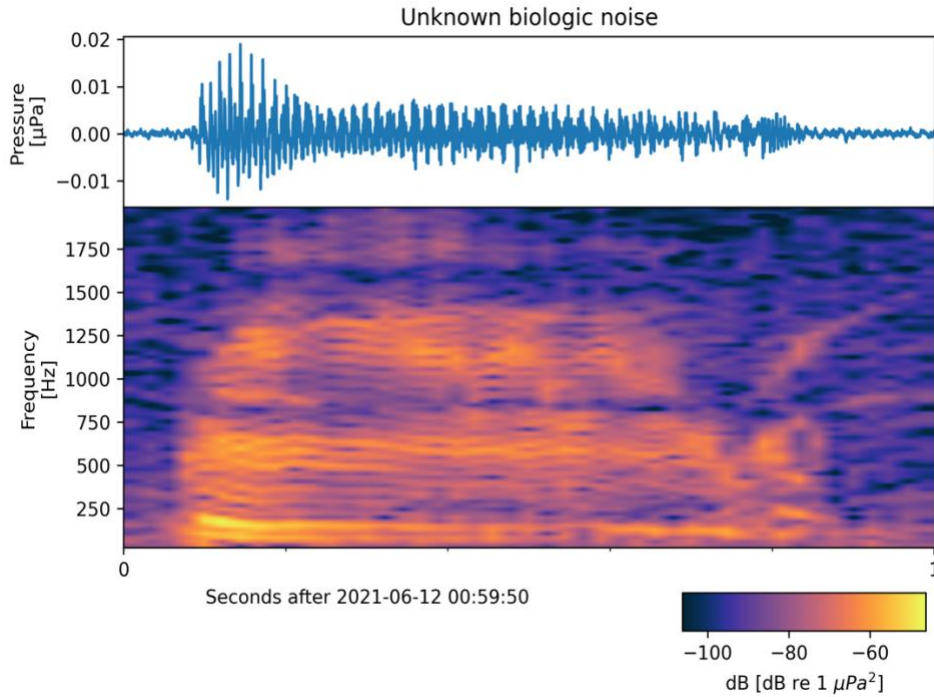


Figure 5.10 Vocalization, unattributed.

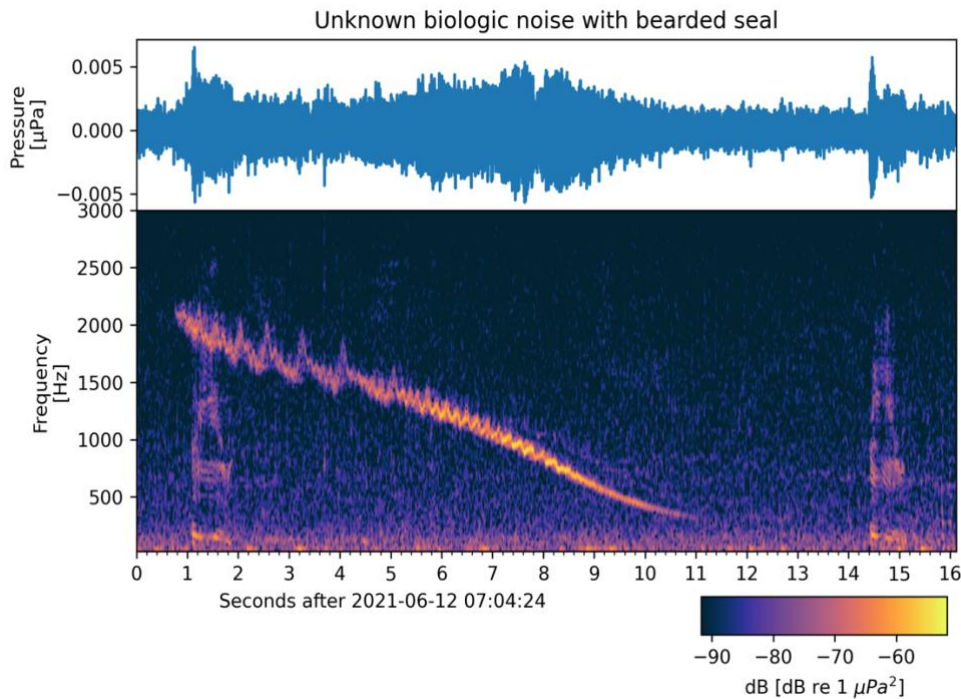


Figure 5.11. *Una* animal calls appear at the beginning and end of the spectrogram, shown with an intervening bearded seal call.

### Whale Vocalizations

On the morning of 12 June, what appear to be several whale vocalizations from two separate animals were observed (Fig. 5.12). The calls were centered at approximately 200 Hz and either had a slight downshift in frequency at the start of the vocalization, or a slight upshift at the end. Additional evidence of whales were audible in the recordings but difficult to identify in spectrograms, even with filtering, due to the low SNR.

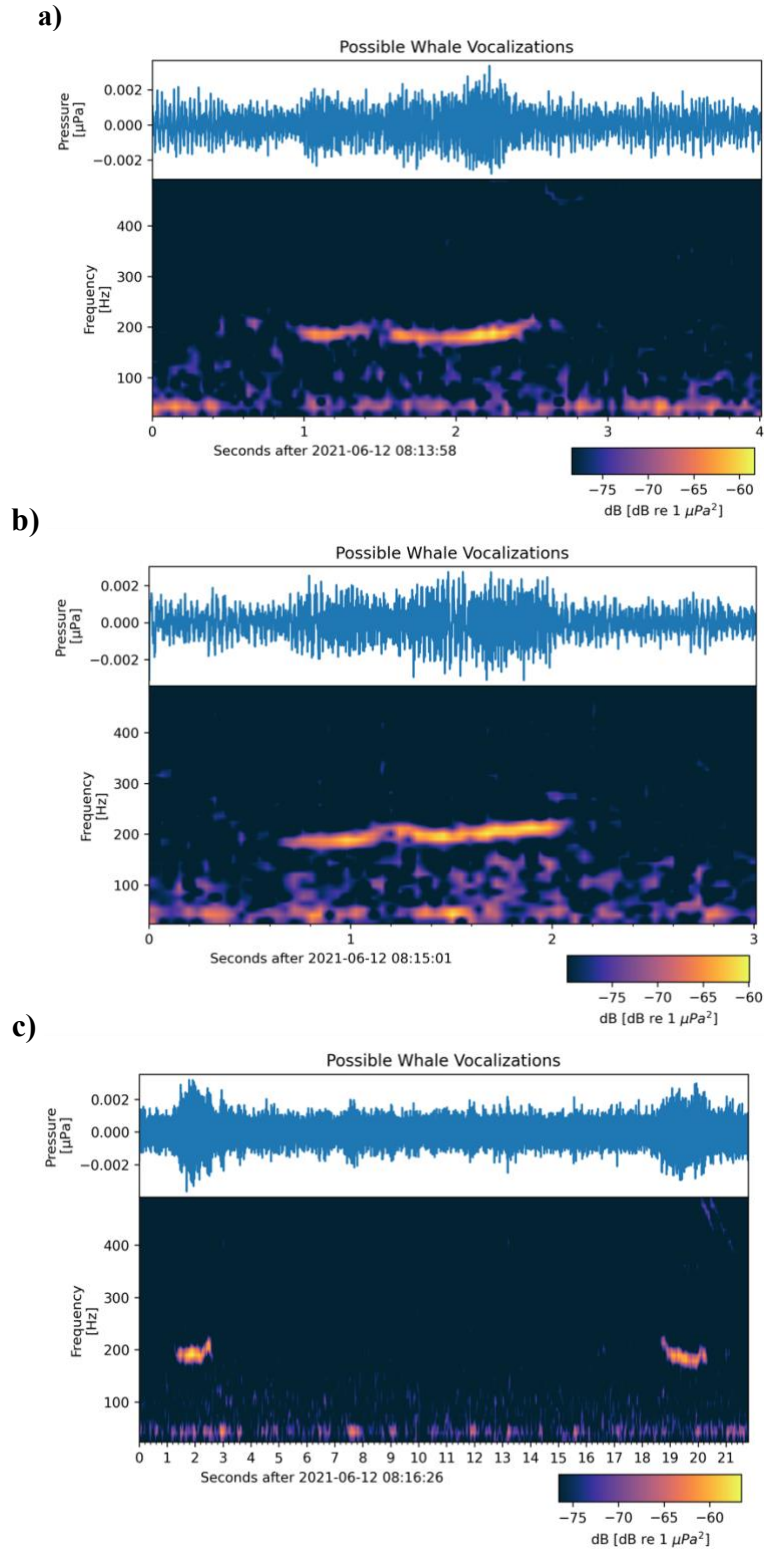


Figure 5.12. Likely whale vocalizations recorded on the morning of 12 June.

## 5.3 ACOUSTIC LOCALIZATION

### 5.3.1 Purpose

Acoustic localization is used in the Arctic to estimate the position of submerged equipment, for example, an oceanographic mooring. In this scenario, active localization is used. During this cruise, two localization experiments were performed, not only to achieve a higher positional accuracy, but to also allow both groups of students to gain experience doing so. Although in this case the floating ice buoy was visible and its GPS location was known, acoustic localization is still necessary to know for submerged moorings and in case of GPS failure.

### 5.3.2 Methodology

Since the students were split up into two groups the experiment was performed twice, with Group A localizing from an approximate 500 m radius circle away from the buoy, and Group B localizing from an approximate 1000 m radius circle away from the buoy. The idea behind acoustic localization is very similar to the idea of triangulation for GPS. If a time that a signal travels to the buoy and back to the ship is taken, a range of how far the buoy is from the ship can be derived, resulting in a circle of position of around the ship of where the buoy should be located. When the ship moves position, and this procedure is conducted at least three times, the resulting intersection is presumed to be the position of the buoy (Send et al. 1995). Since increasing the number of circles of position improved the accuracy of the derived position, the procedure was performed four times by each group.

Since a GPS receiver was mounted to top of the buoy, the position of the buoy was used by KV Svalbard to maneuver within approximately 500 m of the buoy for Group A, and 1000m of the buoy for Group B. Next, an acoustic source, which emitted short pings recognized by the transponder on the buoy, was lowered to 15.5m below the surface of the water. A piece of tape was attached to the wire marking how far the source needed to be lowered so that the depth would be consistent between all measurements. After the transponder was lowered to the correct depth, the position of the ship was recorded and an acoustic signal was sent. The Tx/Rx frequencies used were 11/12 kHz. Once the signal traveled back to the ship from the CAT, the two-way travel time (TWTT) was recorded. The ship was then maneuvered to another position along the 500 m or 1000 m radius around the buoy three more times, with the same procedure repeated for each of those positions.

*Table 5.2. An example of data collection done by Group A.*

Time (UTC)	Ship Position (Latitude)	Ship Position (Longitude)	Two-way Travel Time (ms)
05:02	N 80° 55.3501'	E 010° 13.9118'	851.6
05:15	N 80° 55.1844'	E 010° 16.5782'	656.06
05:35	N 80° 55.4784'	E 010° 18.3356'	865.12
05:53	N 80° 55.5761;	E 010° 16.4029'	795.4

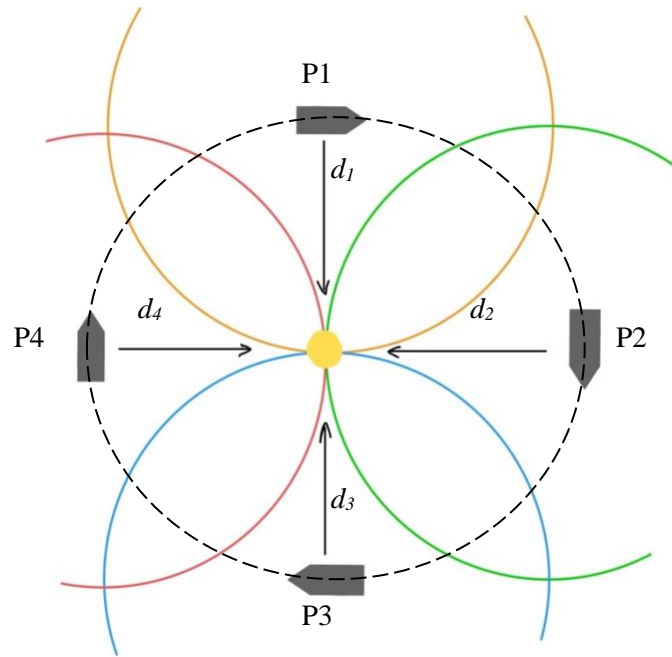


Figure 5.13. Acoustic localization using the theory of triangulation with four positions.

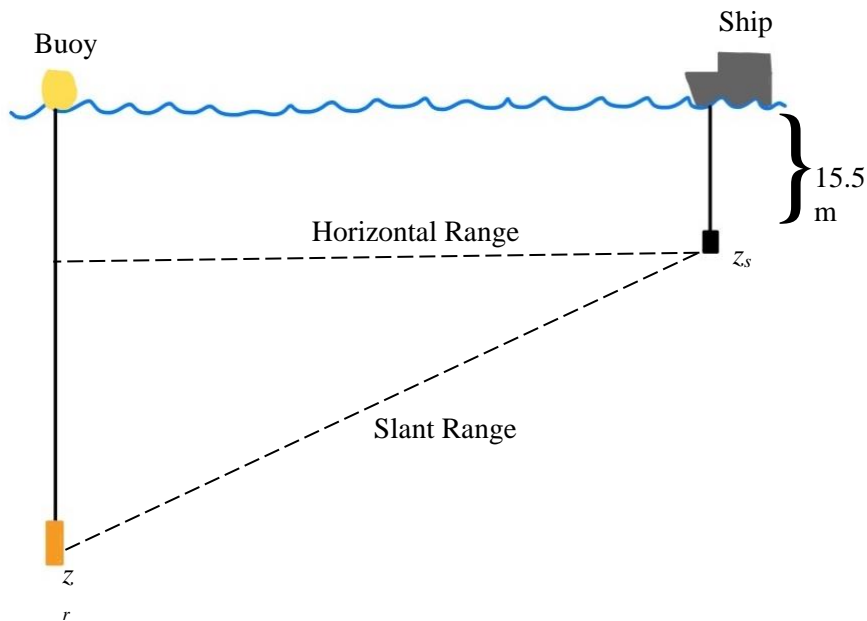


Figure 5.14 Visualization of deriving the horizontal distance between the ship and buoy.

### 5.3.3 Calculations

To derive the slant range, the time it took for the signal to travel one way is needed. Since there was a delay in the signal being transmitted back by the CAT, a time delay ( $T_{\text{delay}}$ ) of 12.5 ms was factored into the calculation.

**Equation 3.1** 
$$T = \frac{TWTT}{2} - T_{\text{delay}}$$

To calculate the slant range, the average sound speed ( $C_{\text{ave}}$ ) of 1442 m/s was used, which was derived from CTD casts done in the area. The slant range, and the vertical distance between the receiver on the ship and the

CAT-pinger on the buoy, which was mounted at 33 m below the surface, were then used to calculate the horizontal range.

**Equation 3.2** 
$$R_{slant} = C_{ave} T$$

**Equation 3.3** 
$$R_{hori} = \sqrt{R_{slant}^2 - |z_r - z_s|^2}$$

### 5.3.4 Results

From the equations above, the four circles of position were constructed for each group. However, both groups were not able to get an exact intersection of either three or four circles, which was necessary in order to derive a precise position. These errors could be due to several factors, the most significant one being that because of the current, neither the ship, nor the transponder, nor the buoy were completely stationary, and all moved at slightly different rates which were not accounted for in the calculations. Despite these errors, the experiment still produced areas of intersection where the buoy has the highest probability of being located. Given the plots of the localization, both groups used their own logic to give their best guesses of where the buoy would be, with a linear rate of ice drift used to estimate the buoy's position at the time of guess for each group. KV Svalbard's track, both group's guesses as well as the hourly GPS positions reported by the buoy can be seen in Figure 5.15. The distance between the guess and the buoy's estimated location for Group A was 70.3 m while for Group B it was 81.5 m. Although these results may not seem very precise, the results were accurate enough for the purposes of acoustic localization.



Figure 5.15. GPS track of KV Svalbard (yellow), guess of Group A (green star), guess of Group B (orange star), and hourly GPS positions of the buoy (red dots). Plot acquired from personal communication.

## 5.4 ICE STATIONS

Additional acoustic measurements were taken with a hydrophone lowered by hand through a hole drilled in the sea ice during sea ice station measurements. Most of the time, mechanical noise from the nearby ship was far louder than any environmental signals that might have been of interest. One exception is the controlled explosion, described here.

### 5.4.1 Taking a Sounding with Explosives

On the evening of 14 June, KV Svalbard stationed herself on a floe located at 82°5'36.43"W, 10°2'10.71"E. Though the main purpose of this visit was to observe ice ridges on the floe, an interesting opportunity for acoustic measurement arose when the ship's crew was given permission to detonate expired explosives. Using one of the many holes drilled for ice ridge observation, a hydrophone was lowered beneath the ice to capture the explosion as heard underwater. The explosives were emplaced in the ice approximately two hundred meters away.

Explosions create an impulsive signal, enabling an estimate of the bottom depth using acoustic travel times. The distance traveled by an acoustic wave is  $d = c \cdot t$ , where  $c$  is the speed of sound and  $t$  is the time elapsed. In this case, since the acoustic signal is traveling to the bottom of the ocean and back,  $t$  is the two-way travel time and must be divided by two to give the bottom depth  $z_b$ :

$$z_b = \frac{c \cdot t}{2}.$$

Because the depth of the ocean is much greater than the distance between the source and receiver at the surface, the source and receiver are assumed to be in the same position. Figure 5.16 shows the normalized acoustic pressure and spectrogram of the recorded signal. The two-way travel time is obtained from the time difference of arrival between the first and second impulses. Using an estimated average sound speed of 1490 m/s and a measured time difference of arrival of 1.293 s, the bottom depth is estimated to be 963 m at this location.

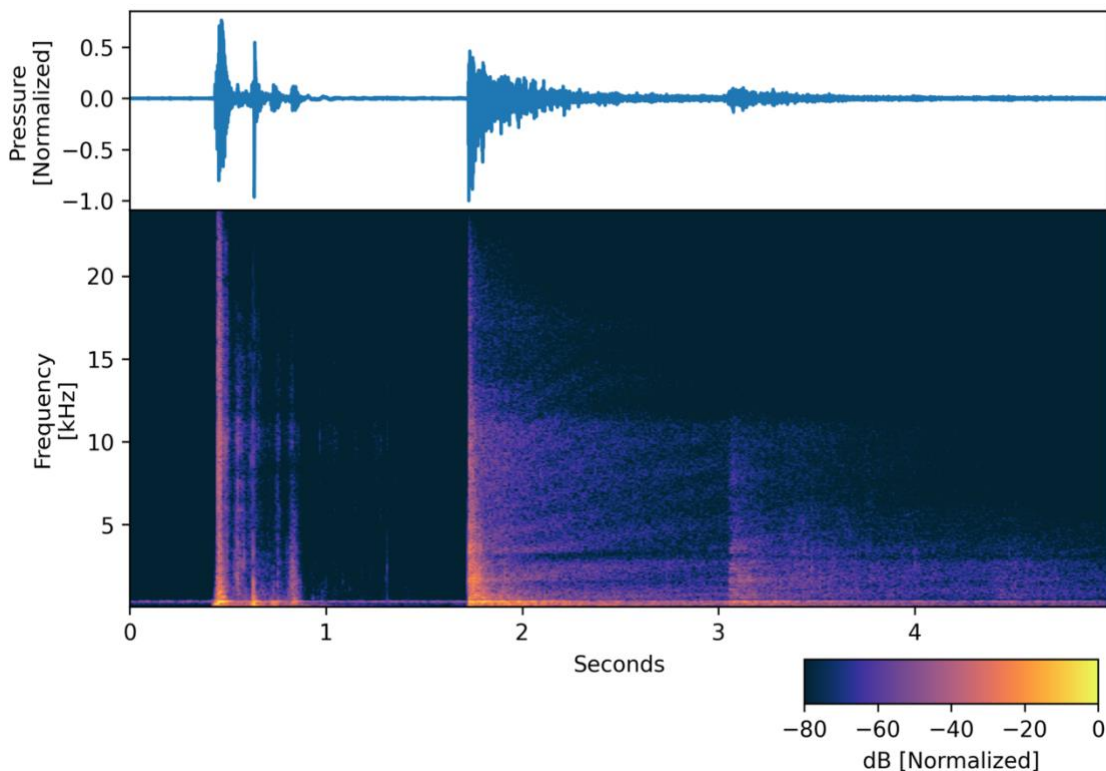


Figure 5.16. Normalized time series and spectrogram of explosives detonation on sea ice, followed by first and subsequent bottom bounce reflections.

Figure 5.16 contains some noteworthy propagation features. The first wave packet appears to contain multiple sub-packets of energy. This is likely a combination of two factors. First, several explosives were detonated, but due to latency in the detonation cord and fuses, they did not detonate simultaneously. The asynchronous detonation was recorded on film and audio by the observers. Second, because the explosives were emplaced within the ice, energy propagates seismo-acoustically through elastic media (the ice) as well as through the water. The speed of propagation for longitudinal waves in ice is approximately 3,800 m/s, and shear waves are approximately 1,800 m/s (Vogt et al.). As these waves propagate outward through the ice, energy along this wavefront is transmitted into the water. These elastic modes of propagation are likely the first arrivals recorded, followed by direct path propagation through water between the source and the receiver. Since the ocean acts as an acoustic waveguide, the second packet of energy exhibits geometric dispersion, with an interference pattern taking shape as bands of energy through time and frequency following the arrival of the impulse. A third, weaker arrival remains impulsive, but is further attenuated and dispersed than the second arrival.



*Figure 5.17 Photo of the detonation under ice*

## 5.5 PROPAGATION MODELING

Throughout the cruise, the unique properties of the Arctic Ocean water column were observed. In addition to the CTD on board the drifting buoy (which sampled at a fixed depth), the ocean environment was measured directly from the ship on numerous occasions using expendable bathythermographs (XBT) and full profiles using a rosette CTD. These profiles revealed an upward refracting environment which tends to support a surface duct in the upper sonic layer. A combination of relatively fresh water combined with water cooled by the Arctic air results in especially slow sound speeds in the upper ocean. Figure 5.18 shows a simplified acoustic propagation model for transmission loss using environmental data collected by an XBT during the acoustic localization exercise. The model (Porter 1992) uses normal modes and wavenumber integration to compute transmission loss for a source positioned at 10.5 m out to a range of 20 km (Figure 5.18a) and 100 km (Figure 5.18b) for a 150 Hz source. Surface ducting is visible in both panels, with the sonic layer depth located at the thermocline at an average depth of approximately 150 m. In Figure 5.18b, the deeper water is also upward refracting, causing sound to bend upwards. This water is too shallow to support convergence zone propagation, but a half channel is clear in Figure 5.18b, as annuli occur approximately every 35 km where sound is reflected off the surface of the ocean/bottom of the ice. This modeling does not take into account surface roughness, which would have a deleterious effect on transmission loss. Nevertheless, the model shows that the most likely paths for propagation are direct path (close range), surface duct (medium range due to the frequent interactions with the ice and surface scattering), and half-channel surface bounce (longer range due to more infrequent interactions with boundaries).

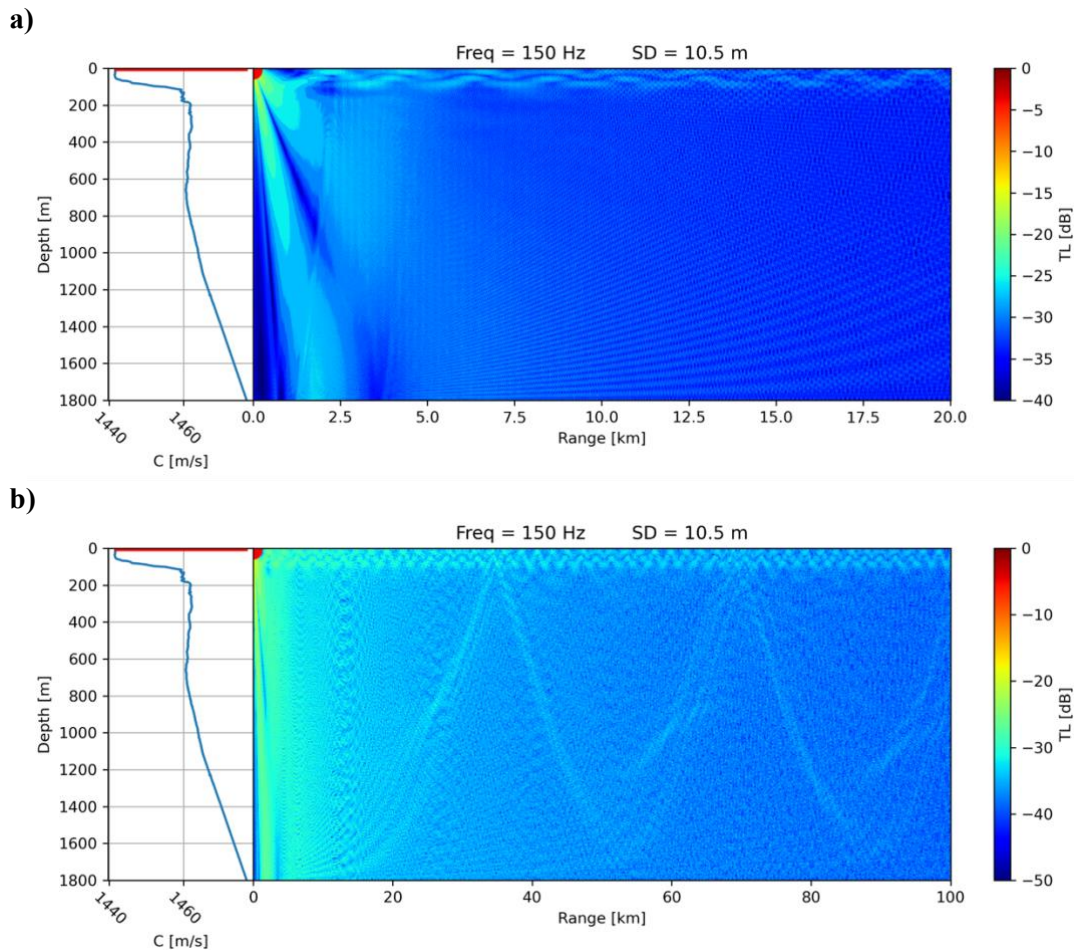


Figure 5.18. Transmission loss for a source at 10.5 m, 150 Hz using KRAKEN normal mode propagation model.

## REFERENCES

- Hersbach, H., Bell, B., Berrisford, P., Biavati, G., Horányi, A., Muñoz Sabater, J., Nicolas, J., Peubey, C., Radu, R., Rozum, I., Schepers, D., Simmons, A., Soci, C., Dee, D., Thépaut, J-N. (2018): ERA5 hourly data on single levels from 1979 to present. Copernicus Climate Change Service (C3S) Climate Data Store (CDS). (Accessed on 07-Jan-2022), <https://doi.org/10.24381/cds.adbb2d47>
- Mahanty, M.M., Latha, G., Venkatesan, R. *et al.* Underwater sound to probe sea ice melting in the Arctic during winter. *Sci Rep* 10, 16047 (2020). <https://doi.org/10.1038/s41598-020-72917-4>
- U. Send, M. Visbeck and G. Krahnemann, "Aspects of acoustic transponder surveys and acoustic navigation," *'Challenges of Our Changing Global Environment'. Conference Proceedings. OCEANS '95 MTS/IEEE*, 1995, pp. 1631-1642 vol.3, <https://ieeexplore.ieee.org/document/528730>
- Porter, M.B. The KRAKEN normal mode program. 1992.
- Christian Vogt, Karim Laihem, and Christopher Wiebusch , "Speed of sound in bubble-free ice", *The Journal of the Acoustical Society of America* 124, 3613-3618 (2008)<https://doi.org/10.1121/1.2996304>
- University of Rhode Island Graduate School of Oceanography. *Discovery of Sound in the Sea (DOSITS)*. University of Rhode Island. <https://dosits.org>
- William Jenkins, Hayden Johnson, Sofia Vakhutinsky, Meghan Nicole Helmberger, Espen Storheim, Hanne Sagen, and Stein Sandven:(2022). Analysis of underwater acoustic data collected under sea ice during the Useful Arctic Knowledge 2021 cruise. *Proc. Mtgs. Acoust.* 47, 070003 (2022); <https://doi.org/10.1121/2.0001574>

## APPENDIX 1: AVAILABLE SATELLITE IMAGES

The following is a list of satellite images (not exhaustive) available during the periods where data was collected at the ice stations. Freely available data can be searched and downloaded from the ESA hubs or other provider of satellite imagery. Other imagery (highlighted in grey) has been collected under license and you should contact one of the project partners to find out if that particular images are available for further distribution.

[Image name] = image available from ESA hubs (eg. <https://scihub.copernicus.eu>)

[Image name] = image not openly available, contact a project partner for access.

### 1. ICE STATION 1

2021-06-10	
05:46	Radarsat-2
RS2_20210610_054633_0076_SCWA_HHHV_SGF_902534_8141_41644443	
07:10	Sentinel-1
S1B_EW_GRDM_1SDH_20210610T071053_20210610T071153_027291_034277_7771	
13:37 - 13:43	Sentinel-2
S2B_MSIL2A_20210610T133729_N0300_R067_T33XXL_20210610T162037	
S2B_MSIL2A_20210610T133729_N0300_R067_T35XML_20210610T162037	
14:27 - 14:28	Sentinel-2
S2A_MSIL2A_20210610T142741_N0300_R139_T33XXL_20210610T170554	
S2A_MSIL2A_20210610T142741_N0300_R139_T35XML_20210610T170554	
14:06	Radarsat-2 (Quad-Pol)
RS2-SLC-FQ9-ASC-10-Jun-2021_14.06-KNOS_41499949	
2021-06-11	
06:57	Radarsat-2
RS2_20210611_065738_0076_SCWA_HHHV_SGF_902719_8160_41660331	
13:07 - 13:11	Sentinel-2
S2B_MSIL2A_20210611T130709_N0300_R081_T33XXL_20210611T141852	
S2B_MSIL2A_20210611T130709_N0300_R081_T35XML_20210611T141852	
13:57 - 13:59	Sentinel-2
S2A_MSIL2A_20210611T135731_N0300_R010_T33XXL_20210611T163734	

S2A_MSIL2A_20210611T135731_N0300_R010_T35XML_20210611T163734	
14:47 - 14:55	Sentinel-2
S2B_MSIL2A_20210611T144749_N0300_R082_T33XXL_20210611T153034 S2B_MSIL2A_20210611T144749_N0300_R082_T35XML_20210611T153034	
15:17	Radarsat-2 (Quad-Pol)
RS2-SLC-FQ24-ASC-11-Jun-2021_15.17-KNOS_41499951	
<b>2021-06-12</b>	
06:28	Radarsat-2
RS2_20210612_062822_0076_SCWA_HHHV_SGF_902936_8174_41682041	
06:54	Sentinel-1
S1B_EW_GRDM_1SDH_20210612T065459_20210612T065559_027320_034357_969C	
13:27 - 13:29	Sentinel-2
S2A_MSIL2A_20210612T132721_N0300_R024_T33XXL_20210612T160618 S2A_MSIL2A_20210612T132721_N0300_R024_T35XML_20210612T160618	
14:17 - 14:26	Sentinel-2
S2B_MSIL2A_20210612T141739_N0300_R096_T33XXL_20210612T152418 S2B_MSIL2A_20210612T141739_N0300_R096_T35XML_20210612T152418	
<b>2021-06-13</b>	
No Coverage	
<b>2021-06-14</b>	
05:50	Sentinel-1
S1A_EW_GRDM_1SDH_20210614T055022_20210614T055126_038332_048610_D9BF	
06:38	Sentinel-1
S1B_EW_GRDM_1SDH_20210614T063839_20210614T063939_027349_03442A_6450	

## 2. ICE STATION 2

<b>2021-06-14</b>	
05:29	Radarsat-2
RS2_20210614_052948_0076_SCWA_HHHV_SGF_903361_8204_41713207	
06:38	Sentinel-1

S1B_EW_GRDM_1SDH_20210614T063839_20210614T063939_027349_03442A_6450	
08:16	Sentinel-1
S1B_EW_GRDM_1SDH_20210614T081627_20210614T081727_027350_034434_082B	
14:57	Sentinel-2
S2B_MSIL2A_20210614T145759_N0300_R125_T33XVM_20210614T192215	
15:29	Radarsat-2
RS2_OK128443_PK1132706_DK1089877_SCWA_20210614_152911_HH_HV_SGF	
15:48	Sentinel-2
S2A_MSIL2A_20210614T154811_N0300_R054_T33XVM_20210614T175833	
<b>2021-06-15</b>	
06:40	Radarsat-2
RS2_20210615_064056_0076_SCWA_HHHV_SGF_903569_8215_41733690	
07:18	Sentinel-1
S1B_EW_GRDM_1SDH_20210615T071907_20210615T072007_027364_0344A6_78A5	
14:27	Sentinel-2
S2B_MSIL2A_20210615T142749_N0300_R139_T33XVM_20210615T152858	
15:18	Sentinel-2
S2A_MSIL2A_20210615T151801_N0300_R068_T33XVM_20210615T174159	
<b>2021-06-16</b>	
06:12	Radarsat-2
RS2_20210616_061205_0076_SCWA_HHHV_SGF_903775_8234_41761215	
06:18	Sentinel-1
S1B_EW_GRDM_1SDH_20210616T080008_20210616T080108_027379_03451E_59A7	
14:27	Sentinel-2
S2A_MSIL2A_20210616T144751_N0300_R082_T33XVM_20210616T204032	
15:18	Sentinel-2
S2B_MSIL2A_20210616T153809_N0300_R011_T33XVM_20210616T201242	

## APPENDIX 2: TABLES OF IN SITU SNOW AND ICE MEASUREMENTS

Table 1.1 Snow pit positions and snow layer depths

Point - Distance	X Distance [m]	Y Distance [m]	Layer [cm]	Top [cm]	Bottom [cm]
S1-1	7	0	62-72	72 cm	62 cm
			52-62	62 cm	52 cm
			42-52	52 cm	42 cm
			32-42	42 cm	32 cm
			22-32	32 cm	22 cm
			12-22	22 cm	12 cm
			0-12	12 cm	0 cm
S1-2	17	0	40-45	45 cm	40 cm
			35-40	40 cm	35 cm
			30-35	35 cm	30 cm
			25-30	30 cm	25 cm
			20-25	25 cm	20 cm
			15-20	20 cm	15 cm
			10-20	15 cm	10 cm
			5-10	10 cm	5 cm
			0-5	5 cm	0 cm
S1-3	4.75	5.45	42-47	47 cm	42 cm
			37-42	42 cm	37 cm
			32-37	37 cm	32 cm
			27-32	32 cm	27 cm
			22-27	27 cm	22 cm
			17-22	22 cm	17 cm
			12-17	17 cm	12 cm
			7-12	12 cm	7 cm
			0-7	7 cm	0 cm
S1-4	21.2	4.49	36-41	41 cm	36 cm
			31-36	36 cm	31 cm
			26-31	31 cm	26 cm
			21-26	26 cm	21 cm
			16-21	21 cm	16 cm
			11-16	16 cm	11 cm
			6-11	11 cm	6 cm
			1-6	6 cm	1 cm
S1-5	11.2	13.5	35-40	40 cm	35 cm
			30-35	35 cm	30 cm
			25-30	30 cm	25 cm
			20-25	25 cm	20 cm
			15-20	20 cm	15 cm
			10-15	15 cm	10 cm
			5-10	10 cm	5 cm
			0-5	5 cm	0 cm
S1-6	22.6	28.8	26-31	31 cm	26 cm
	(37.2)		21-26	26 cm	21 cm
			16-21	21 cm	16 cm

			11-16	16 cm	11 cm
			6-11	11 cm	6 cm
			1-6	6 cm	1 cm
S1-7	24	10	5-10	10 cm	5 cm
			0-5	5 cm	0 cm
S1-8	0	24.8	26-31	31 cm	26 cm
			21-26	26 cm	21 cm
			16-21	21 cm	16 cm
			11-16	16 cm	11 cm
			6-11	11 cm	6 cm
			1-6	6 cm	1 cm

Table 1.2: Snow pit density measurements

Point	Depth Top [cm]	Depth Bottom [cm]	Original weight [g]	Epsilon value	Shovel Size	Snow Density [g/cm <sup>3</sup> ]	Moisture
S1-1	0 cm	10 cm	80.0 g	0	Large	0.4010025	0
	10 cm	20 cm	105.0 g	0	Large	0.5263158	0
	30 cm	40 cm	37.0 g	0	Small	0.3737374	0
	50 cm	60 cm	38.0 g	0	Small	0.3838384	0
S1-2	0 cm	5 cm	42.0 g	0	Small	0.4242424	0
	15 cm	20 cm	43.0 g	0	Small	0.4343434	0
	30 cm	35 cm	45.0 g	0	Small	0.4545455	0
	40 cm	45 cm	36.0 g	0	Small	0.3636364	0
S1-3	5 cm	10 cm	40.0 g	0	Small	0.4040404	0
	20 cm	25 cm	58.0 g	0	Small	0.5858586	0
	35 cm	40 cm	34.0 g	0	Small	0.3434343	0
S1-4	5 cm	10 cm	47.0 g	0	Small	0.4747475	0
	20 cm	25 cm	58.0 g	0	Small	0.5858586	0
	35 cm	40 cm	40.0 g	0	Small	0.4040404	0
S1-5	5 cm	10 cm	62.0 g	0	Large	0.3107769	0
	15 cm	20 cm	74.0 g	0	Large	0.3709273	0
	30 cm	35 cm	68.0 g	0	Large	0.3408521	0
S1-6	10 cm	5 cm	63.0 g	0	Large	0.3157895	0
	20 cm	15 cm	68.0 g	0	Large	0.3408521	0
	30 cm	25 cm	59.0 g	0	Large	0.2957393	0
S1-7	0 cm	5 cm	25.0 g	0	Small	0.2525253	0
	10 cm	15 cm	28.0 g	0	Small	0.2828283	0
S1-8	8 cm	3 cm	40.0 g	0	Small	0.4040404	0
	18 cm	13 cm	40.0 g	0	Small	0.4040404	0
	29 cm	24 cm	40.0 g	0	Small	0.4040404	0

Table 1.3 Snow pit profile temperatures

Point	Depth [cm]	Temp [°C]
S1-1	0 cm	0.2 °C

UAK Research school report 2021

	10 cm	0.1 °C
	20 cm	0.0 °C
	30 cm	0.0 °C
	40 cm	-0.2 °C
	50 cm	-0.5 °C
	60 cm	-1.5 °C
	72 cm	-2.4 °C
S1-2	0 cm	0.1 °C
	5 cm	0.0 °C
	10 cm	0.0 °C
	15 cm	0.0 °C
	20 cm	-0.1 °C
	25 cm	-0.3 °C
	30 cm	-0.7 °C
	35 cm	-1.0 °C
	40 cm	-1.2 °C
	45 cm	-1.9 °C
S1-3	0 cm	0.0 °C
	5 cm	0.1 °C
	10 cm	0.1 °C
	15 cm	0.1 °C
	20 cm	-0.1 °C
	25 cm	-0.2 °C
	30 cm	-0.3 °C
	35 cm	-0.6 °C
	40 cm	-0.8 °C
	47 cm	-1.0 °C
S1-4	0 cm	0.0 °C
	5 cm	0.1 °C
	10 cm	0.1 °C
	15 cm	0.0 °C
	20 cm	0.0 °C
	25 cm	-0.1 °C
	30 cm	-0.3 °C
	35 cm	-0.6 °C
	40 cm	-1.5 °C

S1-5	0 cm	-0.1 °C
	5 cm	0.0 °C
	10 cm	0.0 °C
	15 cm	0.0 °C
	20 cm	0.0 °C
	25 cm	-0.1 °C
	30 cm	-0.2 °C
	35 cm	-0.4 °C
	40 cm	-0.7 °C
S1-6	0 cm	0.1 °C
	5 cm	0.1 °C
	10 cm	0.1 °C
	15 cm	-0.1 °C
	20 cm	-0.3 °C
	25 cm	-0.8 °C

	30 cm	-1.6 °C
S1-7	0 cm	0.0 °C
	5 cm	-0.3 °C
	9 cm	-0.6 °C
S1-8	0 cm	0.0 °C
	5 cm	0.0 °C
	10 cm	0.0 °C
	15 cm	0.0 °C
	20 cm	-0.3 °C
	25 cm	-0.6 °C
	30 cm	-0.9 °C

Table 1.4: Coordinates, snow thickness, freeboard and ice thickness recorded at all drilling locations. Locations T1\_1 to T1\_21 were drilled inside the grid, ROV\_1 to ROV\_11 along the ROV transect, and Ridge2\_B and Ridge2\_C on a ridge.

Drilling location	X [m]	Y[m]	Snow thickness [cm]	Freeboard [cm]	Ice thickness [cm]
T1_1	2.00	0.00	29.00	29.00	138.00
T1_2	2.00	2.00	14.00	14.00	172.00
T1_3	2.00	2.00	17.00	18.00	179.00
T1_4	2.00	2.00	15.00	19.00	140.00
T1_5	2.00	2.00	10.00	19.00	179.00
T1_6	2.00	2.00	4.00	12.00	159.00
T1_7	2.00	2.00	5.00	19.00	174.00
T1_8	6.00	2.00	10.00	9.00	130.00
T1_9	6.00	2.00	19.00	11.00	145.00
T1_10	6.00	2.00	11.00	8.00	135.00
T1_11	6.00	2.00	10.00	9.00	147.00
T1_12	6.00	2.00	7.00	9.00	190.00
T1_13	13.00	2.00	8.00	14.00	142.00
T1_14	21.00	2.00	6.00	22.00	152.00
T1_15	17.00	2.00	3.00	1.00	147.00
T1_16	17.00	2.00	5.00	18.00	154.00
T1_17	22.00	2.00	5.00	17.00	154.00
T1_18	23.00	2.00	4.00	24.00	166.00
T1_19	35.00	2.00	8.00	16.00	157.00
T1_20	32.00	2.00	21.00	2.50	116.00
T1_21	38.00	2.00	19.00	4.25	119.00
ROV_1	29.80	NA	NA	15.00	150.00
ROV_2	25.65	NA	NA	9.00	127.00
ROV_3	22.40	NA	NA	20.00	134.00
ROV_4	19.35	NA	NA	22.00	188.00
ROV_5	15.80	NA	NA	30.00	208.00
ROV_6	12.60	NA	NA	20.00	210.00
ROV_7	9.00	NA	NA	31.00	208.00
ROV_8	6.75	NA	NA	40.00	209.00
ROV_9	3.10	NA	NA	29.00	163.00
ROV_11	-10.00	NA	NA	0.00	172.00
Ridge2_B	NA	NA	18.00	-7.00	248.00
Ridge2_C	NA	NA	NA	-6.00	430.00

Table 1.5 Temperature, salinity and density profiles of cores 1-6

UAK Research school report 2021

Core	Depth [cm]	Temperature [°C]	Salinity [ppt]	Density [kg/m <sup>3</sup> ]
<b>C1</b>	<b>10</b>	<b>-0.9</b>	<b>NA</b>	<b>NA</b>
C1	20	-1	NA	NA
C1	30	-1.5	NA	NA
C1	40	-1.7	NA	NA
C1	50	-1.9	NA	NA
C1	60	-1.6	NA	NA
C1	70	-1.9	NA	NA
C1	80	-2.1	NA	NA
C1	90	-1.9	NA	NA
C1	100	-2.1	NA	NA
C1	110	-2	NA	NA
C1	120	-1.6	NA	NA
C1	130	-1.7	NA	NA
C1	140	-1.6	NA	NA
C1	3.1	NA	1.1	308.0803
C1	10.05	NA	2.3	392.6313
C1	17.55	NA	1.76	444.8174
C1	26.7	NA	4.08	392.6313
C1	37.7	NA	4.1	431.0985
C1	48.7	NA	5	419.4725
C1	58.6	NA	NA	NA
C1	69	NA	4.76	437.7308
C1	79.85	NA	4.35	NA
C1	88.8	NA	3	NA
C1	99.8	NA	3.96	448.5836
C1	110.7	NA	0.18	405.8958
C1	119.95	NA	3.96	383.1987
<b>C2</b>	<b>10</b>	<b>0</b>	<b>NA</b>	<b>NA</b>
C2	20	0	NA	NA
C2	30	-0.3	NA	NA
C2	40	-0.9	NA	NA
C2	50	-1.4	NA	NA
C2	60	-1.5	NA	NA
C2	70	-1.6	NA	NA
C2	80	-1.7	NA	NA
C2	90	-1.7	NA	NA
C2	100	-1.8	NA	NA
C2	2.5	NA	NA	NA
C2	11.5	NA	0.18	646.433
C2	23	NA	0.085	916.7595
C2	39	NA	NA	NA
C2	56.25	NA	3.14	754.1718
<b>C3</b>	<b>15</b>	<b>-0.9</b>	<b>3.5</b>	<b>398.0892</b>
C3	20	-1.1	NA	NA
C3	30	-1.3	NA	NA
C3	40	-1.5	NA	NA
C3	50	-1.7	NA	NA
C3	60	-1.9	NA	NA
C3	70	-1.9	NA	NA
C3	80	-1.9	NA	NA

UAK Research school report 2021

C3	25	NA	2.52	420.3822
C3	35	NA	3.93	426.7516
C3	65	NA	4	433.121
C3	75	NA	4.93	426.7516
<b>C4</b>	<b>0</b>	<b>0.5</b>	<b>NA</b>	<b>NA</b>
C4	10	-0.2	NA	NA
C4	20	-1.3	NA	NA
C4	30	-1.3	NA	NA
C4	40	-1.6	NA	NA
C4	50	-1.9	NA	NA
C4	60	-0.16	NA	NA
C4	70	-0.17	NA	NA
C4	18.25	NA	3.64	763.9663
C4	37	NA	2.4	700.3024
C4	65.5	NA	2.79	891.294
<b>C5</b>	<b>5</b>	<b>-0.4</b>	<b>NA</b>	<b>NA</b>
C5	10	-0.4	NA	NA
C5	15	-0.6	NA	NA
C5	25	-1	NA	NA
C5	30	-1.3	NA	NA
C5	40	-1.5	NA	NA
C5	45	-1.6	NA	NA
C5	4.25	NA	0.5	382.0196
C5	13.5	NA	0.2	394.7536
C5	22.75	NA	0.24	389.5102
C5	30.75	NA	NA	415.9769
C5	37.5	NA	NA	427.4981
C5	44	NA	4.43	454.7853
<b>C6</b>	<b>0</b>	<b>0.2</b>	<b>NA</b>	<b>NA</b>
C6	10	0.3	NA	NA
C6	20	0	NA	NA
C6	30	0	NA	NA
C6	40	0	NA	NA
C6	50	-0.5	NA	NA
C6	65	-0.8	NA	NA
C6	70	-1.1	NA	NA
C6	80	-1.2	NA	NA
C6	5	NA	0.049	445.6895
C6	15.5	NA	NA	416.7487
C6	27	NA	NA	419.1604
C6	38	NA	0.17	394.7536
C6	49	NA	NA	450.9954
C6	65	NA	NA	382.0196
C6	75	NA	1.04	477.5245